# Effects of wind speed and tropospheric height on solar power generation: Energy exploration above ground level

**Article** · January 2023

DOI: 10.1016/j.egyr.2023.04.269



Stephen Ndubuisi Nnamchi
Kampala International University (KIU)



Silagi Wanambwa
Texas Tech University



Musiime Enos Bahati
Kampala International University (KIU)



Tukamuhebwa Richard
Kampala International University (KIU)

Energy Reports 9 (2023) 5166–5182

Contents lists available at ScienceDirect

Energy Reports

journal homepage: www.elsevier.com/locate/egyr

Research paper

# Effects of wind speed and tropospheric height on solar power generation: Energy exploration above ground level

Stephen Ndubuisi Nnamchi [a,*], Faith Natukunda [b], Silagi Wanambwa [c], Enos Bahati Musiime [d], Richard Tukamuhebwa [a], Titus Wanazusi [a], Emmanuel Ogwal [e]

[a] Department of Mechanical Engineering, SEAS, Kampala International University, P.O. Box 20000, Kampala, Uganda
[b] Department of Mechanical and Industrial Engineering, Mbarara University of Science and Technology, Uganda
[c] Department of Energy, Mineral and Petroleum Studies, Mbarara University of Science and Technology, Uganda
[d] Department of Civil Engineering, SEAS, Kampala International University, P.O. Box 20000, Kampala, Uganda
[e] Department of Electrical, Telecommunication and Computer Engineering, SEAS, Kampala International University, P.O. Box 20000, Kampala, Uganda

ARTICLE INFO

*Article history:*
Received 25 September 2022
Received in revised form 3 March 2023
Accepted 12 April 2023
Available online xxxx

*Keywords:*
Percentage of solar power gain
Wind speed
Tropospheric height
Modeling
Simulation

ABSTRACT

Terrestrial and extraterrestrial factors hinder the exploitation of solar power using a ground platform. This paper is concerned with the generation of solar power above ground level. This paper employs modeling and simulations coupled with experimentation to establish a functional relationship between the percentage of solar power gain, tropospheric height, and wind speed. The finite difference method based on the Cranks–Nicolson scheme was used to realize the model solution. The wind flow equation established a linear relationship between tropospheric height and wind speed, between tropospheric height and the percentage of solar power gain. It is evident that an infinitesimal percentage of solar power gain (≈2.5%) corresponded to 1000 m above ground level; the tropospheric height of 8100 m recorded 23% of solar power gain. Furthermore, wind speeds of 0 to 33 $ms^{-1}$/distance (1000 m) correspond to ground level and tropospheric height of about 8100 m respectively. However, there is a prospect of achieving more percentage of solar power gain by applying high-altitude platforms. The results obtained apply to other study areas having elevations close to 1100 m, it serves as a guide in the estimation of the percentage of solar power gain by the virtue of tropospheric height and wind speed.



## 1. Introduction

The socio-economic development of regions and sub-regions depends on the ability of the regions and sub-regions to have self-sustained clean energy generation. Nowadays, it is imperative to explore and exploit clean energy resources of regions and sub-regions in order to have sustainable socio-economic growth in the regions (Tucho and Kumsa, 2020; Rublev et al., 2021; Bishoge et al., 2018). Pertinently, Owusu and Asumadu-Sarkodie (2016) assert the need for energy and its related services to satisfy social and economic development, welfare and health in different regions of the world is perpetually on the increase. Among the renewable energy resources available for satisfying the global energy demand, solar-photovoltaic energy resources and technology remain the most accessible, affordable and sustainable clean energy sources (Maka and Alabid, 2022; Thadani and Go, 2021; Majid, 2020; Bogdanov et al., 2021).

Hence, solar panels are more likely to be efficient at high altitudes because solar radiation increases with altitude in the atmosphere (about 8 – 12%/304.8 m) and atmospheric temperature is low with increasing wind speed to induce fast cooling of the solar panels due to decrease in air molecules, emissions and air temperature. Maximizing radiation and minimizing temperature leads to optimum power generation in solar panels (Chandra et al., 2018), these conditions are favored by high altitudes (Eyring and Kittner, 2022; Baldock and Mokhtarzadeh-Dehghan, 2006; Bhattacharya et al., 2014).

Moreover, the intensity of solar irradiance on a solar panel hinges on the zenith angle and the relative distance of the sun to the earth (Zhang et al., 2021). Blumthaler et al. (1997) observed the magnitude of increase in irradiance with altitude; the daily total of global irradiance ranged between 8%±2% per 1000 m (total irradiance), whereas ultraviolet irradiance ranged between 9%±2% per 1000 m in a clear sky condition. Furthermore, an increase or decrease in the distance between the sun and earth relative to the mean distance between the sun and earth induces

* Corresponding author.
*E-mail addresses:* stephen.nnamchi@kiu.ac.ug (S.N. Nnamchi), fnatukunda@must.ac.ug (F. Natukunda), swanambwa@must.ac.ug (S. Wanambwa), enos.musiime@kiu.ac.ug (E.B. Musiime), tukamuhebwa@kiu.ac.ug (R. Tukamuhebwa), titus.wanazusi@kiu.ac.ug (T. Wanazusi), emmanuel.ogwal@kiu.ac.ug (E. Ogwal).

https://doi.org/10.1016/j.egyr.2023.04.269

high or low solar radiation on a horizontal surface, respectively (Pielke Sr, 2013). In addition, it is phenomenal that whenever the sun is overhead, the earth experiences the maximum intensity of solar radiation, thus, the solar panel outputs peak power (Zakšek et al., 2005; Amaya, 2019).

Uncertainly, Amusan and Igbudu (2014) assert that height has no significant impact on the PV power output. The methodology for investigating the impact of height was deficient in the control experiment, there was no second panel placed on the ground level to simultaneously record power at the ground level. They varied the height of PV from 0 to 4.68 m and recorded ideal power every 15 min, not considering that insolation is not constant. Thus, there should have been an unshaded control panel placed on the ground to simultaneously record the ideal power at zero level and the second panel to track ideal power at any given height, this technique would have demystified or debunked their assertion.

Contrarily, in characterizing the influence of installation height and a green roof on PV performance of ground platforms, Osma et al. (2016) emphasize that a lower height (about 0.5 m above a roof) increases PV performance by 1%, and 2% by a green roof, whereas both increases the PV performance by 2.8%. This is a micro power gain compared to macro power gain in the high altitudes (above the troposphere), however, the height of the green roof is uncertain, thus, neglecting the impact of height on the power gain. Panjwani and Narejo (2014) observed that by placing a panel at an altitude/height of 90 ft/27.432 m power accession of 7%–12% was gained. This result is authenticated by a ground control experiment running simultaneously with an elevated experiment. At higher altitudes, we get more direct irradiation and little diffused radiation, which increases the output power because the inhibiting factors are minimal, however, the lifespan of the photovoltaic panel is reduced and the cost of installation is high (Sodhi et al., 2022). Asgharzadeh et al. (2018) showed that there is a corresponding gain in PV output power below the unspecified saturation height, subsequently, height does not impact the PV output power. However, this conclusion is not supporting the development of high-altitude platforms, HAP, which explore energy beyond the tropospheric or saturation height. Few works support that high altitude engenders more photovoltaic output power (Aglietti et al., 2008; Panjwani and Narejo, 2014). Alrwashdeh (2018) affirms that optimizing the height of the tower supporting a solar panel facilitates greater power production. Chitturi et al. (2018) showed that at a height of 1764 m that the efficiency of solar panels increases by 42% compared to the ones placed at a height of 612 m above sea level. Besides the impact of height, a previous study (Shastry and Arunachala, 2020) supports that cooling of photovoltaic panels enhances their output power. According to Sharaf et al. (2022) cooling could be active (Hassan et al., 2021; Deokar et al., 2021; Dwivedi et al., 2020), passive (Ramkiran et al., 2021; Rakino et al., 2019; Wu and Xiong, 2014), phase change material, PCM (Sahu et al., 2021; Hasan et al., 2017; Seto et al., 2021) and additive PCM (Mahdi et al., 2021; Luo et al., 2017; Atkin and Farid, 2015) aimed at increasing photovoltaic output power. Significantly, cold air is found in the higher atmosphere boosting the performance of HAP. Due to the abundance of air within and beyond tropospheric Height, the present study will be limited to the passive cooling of photovoltaic panels using natural air.

In order to utilize the solar energy available in the high atmosphere, it is necessary to have a high-altitude platform (HAP) or high-altitude aerostatic platform to support appropriate photovoltaic panels (Chitturi et al., 2018; Aglietti et al., 2008; Gupta et al., 2019) could be heavier-than-air (fixed wing airplane) or lighter-than-air (Balloons, Airships, and Propulsion Assisted High-Altitude Platform — PAHAP). Pertinently, this HAP could access solar power to the tune of 25 km, which is above the tropospheric height the present work is studying. Based on the literature considered, there is hardly any that has shown progressive power gain as the altitude increases. With the exception of Panjwani and Narejo (2014) most works in literature, employed uncontrolled experiments to measure only near-ground parameters (power and power gain), whereas some used HAP to measure power in the troposphere and beyond. However, the present work employs modeling and simulation of airflow and practical measurement of ideal power to establish the progressive solar power gain up to an altitude of 9200 m and air speed of 42 m/s according to radiosonde data (Kräuchi and Philipona, 2016) in Fig. 1.

The Navier Strokes equation applies to three-dimensional (3-D) modeling and simulation of fluid potential in a flowing system (Burmasheva and Prosviryakov, 2022; Loria, 2020; Ahammad et al., 2019; Oko and Nnamchi, 2013). Inclusively, Nnamchi et al. (2021) demonstrated the practical application of the Navier Strokes equation in solar-biomass drying. Phenomenally, the present work extends the application of the Navier–Stokes equation to the modeling and simulation of tropospheric wind speeds and tropospheric solar power gain in photovoltaic panels. The Navier Stokes equation for fluid flow applies to solar power gain as this potential replaces vertical wind speed in a boundary value problem emanating from the Navier Stokes equation. The contour analysis of the percentage of solar power gain demonstrates the impact of tropospheric height and wind speed on the percentage of solar power gain. The application of validated model results becomes inevitable and veritable when the measurement is difficult in a remote atmosphere close to the sun.

Therefore, the present work via controlled experiments, modeling, and simulations establishes a practical relationship; between the tropospheric height and wind speed, between the tropospheric height and percentage of solar power gain, and further presents effective solar power gain as a function of tropospheric height and wind speed from the ground level to prospective altitude, which supports progressive solar energy exploitation above the ground level.

## 2. Materials and method

This paper uses both analysis and experimentation to accomplish the objectives of this work outlined in Section 1. Model formulation and simulations portray the analysis of wind flow and the percentage of solar power gain in the study areas.

### 2.1. Map of the study area

The study (practical measurement) was carried out at the Western Campus of Kampala International University, Uganda. Fig. 2 shows the map of the study areas. However, the analysis covered the four regions of Uganda; the Northern region (NR), the Eastern Region (ER), the Central Region (CR), and the Western Region (WR) at elevations of 1073, 1143, 1200, and 1473 m, respectively. Uganda is a Sub-Sahara country situated in East Africa, landlocked by South Sudan in the north, Kenya in the east, the Democratic Republic of the Congo in the west, and Tanzania/Rwanda in the south. Uganda occupies a total land mass of 241559 (sq.km); the NR, ER, CR, and WR cover 82099, 39479, 61403, and 55277 (sq.km), respectively. The major power supply to the national grid is via hydropower generation, 743 MW, which is complemented by ground-level solar power generation in NR (none), ER (Tororo plant; 32000 panels with a generation capacity of 10 MW, Busitema plant with a generation capacity of 4 MW; Mayuge plant 30600 panels with a generation capacity of and Soroti plant; 32680 panels with a generation capacity of

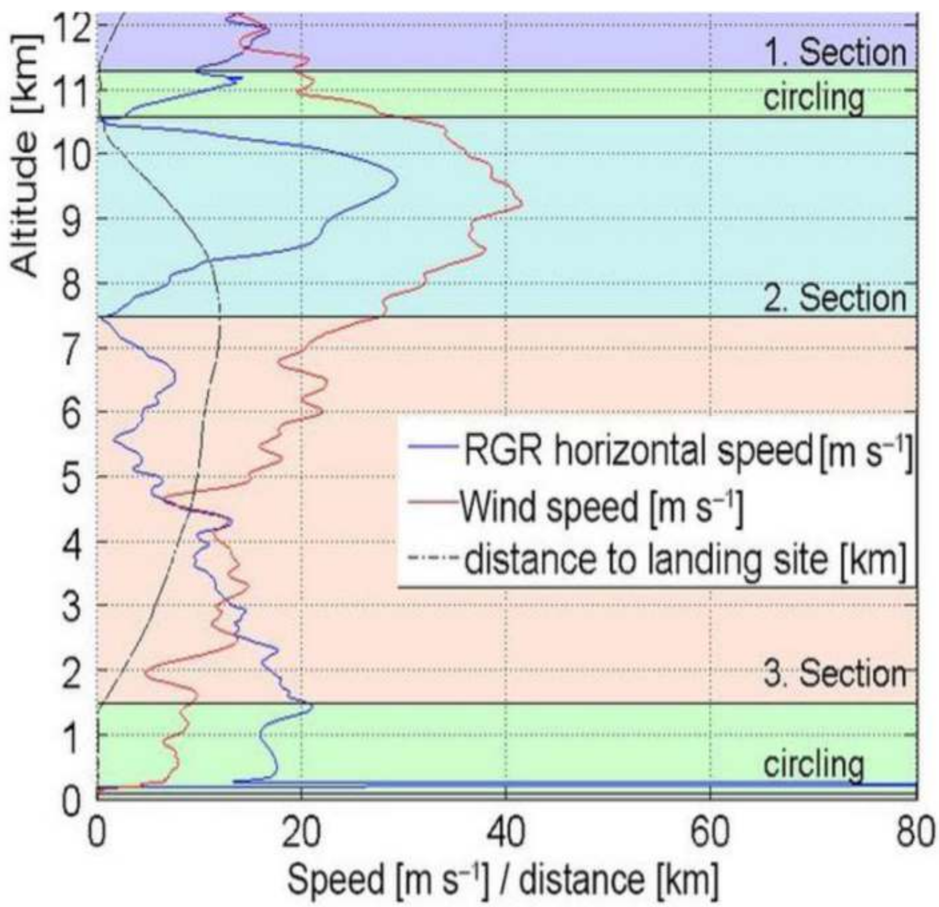


**Fig. 1.** Altitude versus wind speed based on radiosonde (Kräuchi and Philipona, 2016) https://creativecommons.org/licenses/by/4.0/.

10MW), CR (Kabulasoke plant; 68000 solar panels with a generation capacity of 20 MW) Nnamchi et al. (2022) and WR (none). Thus, solar power generated from the two regions (ER and CR) is approximately 50 MW. Western Region has no ground platform partly due to the sloping nature of the region, low average wind speed (5.8 km/h), and least irradiance according to Mundu et al. (2022). Despite these disadvantageous factors, the present work looks into the prospect of exploring solar power above ground level, in this region and other regions, and the introduction of high-altitude platforms in Uganda.

### 2.2. Experiments

Three elevated stations within the Western Campus of Kampala International University were chosen; the Engineering Complex (station 1), the Hostel Complex (station 2), and the Library complex (station 3). The depressed or reference station is the Convocation ground under construction. Two photovoltaic panels (Mira Cozy PV modules; MC010W-18P) were used to measure ideal electric power; the short circuit current (SC) and open circuit voltage (OC) with the aid of Pocket Digital Multi-Meters (MASTECH M830BZ, IEC 61010-1, ±1.2%). By connecting the terminals of the solar panel and the multi-meter, a consecutive measurement of direct current (DC, SC) and direct voltage (DV, OC) was feasible. For the purposes of tracking the percentage of solar power gain, a solar panel was kept at an elevated height, whereas the second solar panel was placed in an unshaded and depressed position. Readings were simultaneously taken at an interval of 15 min when the sun is on noonday (between 1:00 to 2:00 PM). A Surveying Steel tape (BESTIR 01702, 50 m, ±0.03 inch) was used to measure the height of the elevated position from the unshaded and depressed position. The vertical height was measured directly, the sloped height was determined by measuring the slope length, a protractor (Helix H01, ±0.25°) was used to determine the slope angle and right-angle geometry was used to calculate the corresponding sloping height. Thus, the true vertical height is the summation of the sloping height and the vertical height of the structures used to place the elevated solar panel. The experiment was observed for six months only on noonday for the purpose of having appreciable and regular readings. The experiment was observed every 15-min interval, the DC current and voltage were measured and the average values were taken. The percentage of power gain was determined by computing the difference between elevated and depressed solar panel electric powers. A simple multiple linear regression model percentage of power gain against tropospheric height and wind velocity was developed. The measured percentage of power gain validates the simulated one. The pictures of the experimental setup are shown in Fig. 1. The practical wind speed was gotten from radiosonde data after subtracting the elevation of the study areas from the altitude corresponding to the first peak height of the wind speed of about 9200 m (≡ 42 m $s^{-1}$/distance 1000 m) in Figs. 3(a,b,c). The near-ground measured average wind speed data obtained from radiosonde (Kräuchi and Philipona, 2016) was compared with meteorological data (AccuWeather.com, 2022) ranging from 2.22–3.61 m/s. The contours of the percentage solar power gain as a function of tropospheric height and wind speed were developed by plotting the three variables in OriginPro Lab.

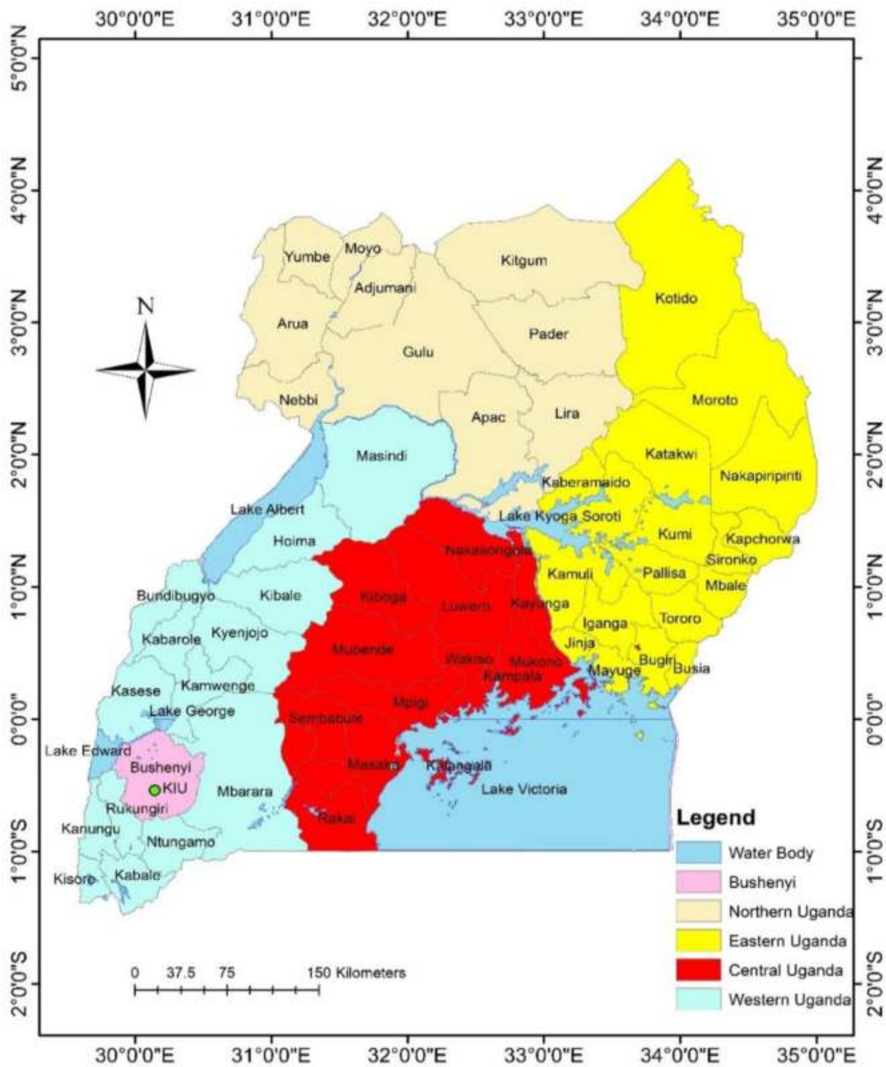


**Fig. 2.** Map of the study areas.

*2.3. Model and numerical formulation of wind flow*

Wind flows are formulated in three dimensions (x,y,z) like any other fluids. Navier Stokes model describes a fluid flow in three dimensions, 3-D (Radwan et al., 2021). Including physical forces; gravity force, GF (Rapp, 2016), pressure gradient force, PGF (Taha and Gonzalez, 2022) and excluding Coriolis force, CF (Lee et al., 2017), the flow describes the wind flow (WF), Wind flow equation (WFE) comprises a local acceleration of the fluid, convective fluid flow diffusive and external force terms in Eq. (1a)

$$\frac{\partial u_x}{\partial t} + u_x\frac{\partial u_x}{\partial x} + u_y\frac{\partial u_x}{\partial y} + u_z\frac{\partial u_x}{\partial z} = g_x - \frac{1}{\rho}\frac{\partial P}{\partial x} + \upsilon\left(\frac{\partial^2 u_x}{\partial x^2} + \frac{\partial^2 u_x}{\partial y^2} + \frac{\partial^2 u_x}{\partial z^2}\right) \quad \exists \quad \upsilon = \frac{\mu}{\rho} \tag{1a}$$

where $u_x$ (m/s) is the component wind velocity in the $x$-direction, $u_y$ (m/s) is the component wind velocity in the $y$-direction, $u_z$ (m/s) is the component wind velocity in the $z$-direction, $t$ (s) is the time, $\mu$ (kg/ms) is the dynamic viscosity of the wind, $\rho$ $\left(\text{kg/m}^3\right)$ is the density of the wind, $\upsilon$ $\left(\text{m}^2/\text{s}\right)$ is the kinematic viscosity of the wind, $g$ $\left(\text{m/s}^2\right)$ is the acceleration due to gravity and $P$ (kPa) is the fluid pressure.

Similarly, WFE in the $y$-direction is presented in Eq. (2a) as

$$\frac{\partial u_y}{\partial t} + u_x\frac{\partial u_y}{\partial x} + u_y\frac{\partial u_y}{\partial y} + u_z\frac{\partial u_y}{\partial z} = g_y - \frac{1}{\rho}\frac{\partial P}{\partial y} + \frac{\mu}{\rho}\left(\frac{\partial^2 u_y}{\partial x^2} + \frac{\partial^2 u_y}{\partial y^2} + \frac{\partial^2 u_y}{\partial z^2}\right) \quad \exists \quad \upsilon = \frac{\mu}{\rho} \tag{2a}$$

where $u_y$ (m/s) is the component wind velocity in the $y$-direction. WFE in the $z$-direction is presented in Eq. (3a) as

$$\frac{\partial u_z}{\partial t} + u_x\frac{\partial u_z}{\partial x} + u_y\frac{\partial u_z}{\partial y} + u_z\frac{\partial u_z}{\partial z} = g_z - \frac{1}{\rho}\frac{\partial P}{\partial z} + \frac{\mu}{\rho}\left(\frac{\partial^2 u_z}{\partial x^2} + \frac{\partial^2 u_z}{\partial y^2} + \frac{\partial^2 u_z}{\partial z^2}\right) \quad \exists \quad \upsilon = \frac{\mu}{\rho} \tag{3a}$$

where $u_z$ (m/s) is the component wind velocity in the $z$-direction.

Imposing steady state condition on Eqs. (1a)–(3a), Eigenvector models are developed in Eqs. (1b)–(3b), then, the steady-state of Eq. (1a) is given in Eq. (1b) as

$$u_x\frac{\partial u_x}{\partial x} + u_y\frac{\partial u_x}{\partial y} + u_z\frac{\partial u_x}{\partial z} = g_x - \frac{1}{\rho}\frac{\partial P}{\partial x} + \upsilon\left(\frac{\partial^2 u_x}{\partial x^2} + \frac{\partial^2 u_x}{\partial y^2} + \frac{\partial^2 u_x}{\partial z^2}\right) \quad \exists \quad \upsilon = \frac{\mu}{\rho} \tag{1b}$$


**Fig. 3.** (a)–(c) Measurement sites.

Similarly, the steady-state of Eq. (2a) is expressed in Eq. (2b) as

$$u_x \frac{\partial u_y}{\partial x} + u_y \frac{\partial u_y}{\partial y} + u_z \frac{\partial u_y}{\partial z} = g_y - \frac{1}{\rho}\frac{\partial P}{\partial y} + \frac{\mu}{\rho}\left(\frac{\partial^2 u_y}{\partial x^2} + \frac{\partial^2 u_y}{\partial y^2} + \frac{\partial^2 u_y}{\partial z^2}\right) \quad \exists \quad \upsilon = \frac{\mu}{\rho} \tag{2b}$$

In the same vein, the steady-state of Eq. (3a) is written in Eq. (3b) as

$$u_x \frac{\partial u_z}{\partial x} + u_y \frac{\partial u_z}{\partial y} + u_z \frac{\partial u_z}{\partial z} = g_z - \frac{1}{\rho}\frac{\partial P}{\partial z} + \frac{\mu}{\rho}\left(\frac{\partial^2 u_z}{\partial x^2} + \frac{\partial^2 u_z}{\partial y^2} + \frac{\partial^2 u_z}{\partial z^2}\right) \quad \exists \quad \upsilon = \frac{\mu}{\rho} \tag{3b}$$

The principle of conservation of fluid mass (the continuity equation) in Eq. (4) supports the validity of the flow equation, Eqs. (1a), (2a), (1b), (2b),

$$\frac{\partial u_x}{\partial x}+\frac{\partial u_y}{\partial y}+\frac{\partial u_z}{\partial z}=0 \tag{4}$$

The pressure gradients in Eqs. (1b), (2b), (3b) are approximated as a product of fluid density and square of its velocity in Eq. (5)

$$\frac{1}{\rho}\frac{\partial P}{\partial x}\approx 0.5\frac{u_x^2}{x};\ \frac{1}{\rho}\frac{\partial P}{\partial y}\approx 0.5\frac{u_y^2}{y};\ \frac{1}{\rho}\frac{\partial P}{\partial z}\approx 0.5\frac{u_z^2}{z} \tag{5}$$

The linear relationship between the component wind velocities and step changes is approximated in Eq. (6)

$$\begin{aligned}
&\frac{u_x}{u_y}\approx-\frac{\Delta x}{\Delta y},\ \frac{u_x}{u_z}\approx-\frac{\Delta x}{\Delta z}\Rightarrow u_x=-\frac{\Delta x}{\Delta y}u_y\,,\\
&u_x=-\frac{\Delta x}{\Delta z}u_z\ \ \exists\ \ \frac{\partial u_x}{\partial x}+\frac{\partial u_y}{\partial y}=0\ \text{ and }\ \frac{\partial u_x}{\partial x}+\frac{\partial u_z}{\partial z}=0\\
&\frac{u_y}{u_x}\approx-\frac{\Delta y}{\Delta x},\ \frac{u_y}{u_z}\approx-\frac{\Delta y}{\Delta z}\Rightarrow u_y=\frac{\Delta y}{\Delta x}u_x\,,\\
&u_y=\frac{\Delta y}{\Delta z}u_z\ \ \exists\ \ \frac{\partial u_x}{\partial x}+\frac{\partial u_y}{\partial y}=0\ \text{ and }\ \frac{\partial u_y}{\partial y}+\frac{\partial u_z}{\partial z}=0\\
&\frac{u_z}{u_x}\approx-\frac{\Delta z}{\Delta x},\ \frac{u_z}{u_y}\approx-\frac{\Delta z}{\Delta y}\Rightarrow u_z=-\frac{\Delta z}{\Delta x}u_x\,,\\
&u_z=-\frac{\Delta z}{\Delta y}u_y\ \ \exists\ \ \frac{\partial u_x}{\partial x}+\frac{\partial u_z}{\partial z}=0\ \text{ and }\ \frac{\partial u_y}{\partial y}+\frac{\partial u_z}{\partial z}
\end{aligned} \tag{6}$$

Substituting Eqs. (5) and (6) into Eqs. (1b)–(3b) yields the modified WFE in Eqs. (7)–(9) respectively with one dependent variable.

$$\begin{aligned}
&u_x\left(\frac{\partial u_x}{\partial x}-\left(\frac{\Delta y}{\Delta x}\right)\frac{\partial u_x}{\partial y}-\left(\frac{\Delta z}{\Delta x}\right)\frac{\partial u_x}{\partial z}\right)=-0.5\frac{u_x^2}{x}\\
&\quad+\upsilon\left(\frac{\partial^2 u_x}{\partial x^2}+\frac{\partial^2 u_x}{\partial y^2}+\frac{\partial^2 u_x}{\partial z^2}\right)\ \ \exists\ \ g_x=0,\quad \upsilon=\frac{\mu}{\rho}
\end{aligned} \tag{7}$$

and

$$\begin{aligned}
&u_y\left(-\left(\frac{\Delta x}{\Delta y}\right)\frac{\partial u_y}{\partial x}+\frac{\partial u_y}{\partial y}-\left(\frac{\Delta z}{\Delta y}\right)\frac{\partial u_y}{\partial z}\right)=-0.5\frac{u_y^2}{y}\\
&\quad+\frac{\mu}{\rho}\left(\frac{\partial^2 u_y}{\partial x^2}+\frac{\partial^2 u_y}{\partial y^2}+\frac{\partial^2 u_y}{\partial z^2}\right)\ \ \exists\ \ g_y=0,\upsilon=\frac{\mu}{\rho}
\end{aligned} \tag{8}$$

and

$$\begin{aligned}
&u_z\left(-\left(\frac{\Delta x}{\Delta z}\right)\frac{\partial u_z}{\partial x}-\left(\frac{\Delta y}{\Delta z}\right)\frac{\partial u_z}{\partial y}+\frac{\partial u_z}{\partial z}\right)=g_z-0.5\frac{u_z^2}{z}\\
&\quad+\frac{\mu}{\rho}\left(\frac{\partial^2 u_z}{\partial x^2}+\frac{\partial^2 u_z}{\partial y^2}+\frac{\partial^2 u_z}{\partial z^2}\right)\ \ \exists\ \ \upsilon=\frac{\mu}{\rho}
\end{aligned} \tag{9}$$

Considering vertical wind flow; Eqs. (7) and (8) vanish as $u_x$ and $u_y$ become zero. Also, wind flow gradient in $z$-direction becomes zero ($\partial/\,\partial z\neq 0$), thus, Eq. (9)) reduces to Eq. (10a)

$$\begin{aligned}
&u_z\left(-\left(\frac{\Delta x}{\Delta z}\right)\frac{\partial u_z}{\partial x}-\left(\frac{\Delta y}{\Delta z}\right)\frac{\partial u_z}{\partial y}\right)=g_z-0.5\frac{u_z^2}{z}\\
&\quad+\frac{\mu}{\rho}\left(\frac{\partial^2 u_z}{\partial x^2}+\frac{\partial^2 u_z}{\partial y^2}\right)\ \ \exists\ \ \upsilon=\frac{\mu}{\rho}
\end{aligned} \tag{10a}$$

The wind speed potential $u_z$ in Eq. (10a) is substituted with percentage power gain, $p_z$ (%) in Eq. (10b)

$$\begin{aligned}
&u_z\left(-\left(\frac{\Delta x}{\Delta z}\right)\frac{\partial p_z}{\partial x}-\left(\frac{\Delta y}{\Delta z}\right)\frac{\partial p_z}{\partial y}\right)=g_z-0.5\frac{u_z^2}{z}\\
&\quad+\frac{\mu}{\rho}\left(\frac{\partial^2 p_z}{\partial x^2}+\frac{\partial^2 p_z}{\partial y^2}\right)\ \ \exists\ \ p_z=\frac{100\left(p_{z,top}-p_{z,base}\right)}{p_{z,base}}\ (\%)
\end{aligned} \tag{10b}$$

where $p_{z,top}$ ($W$) is the power above the ground level and $p_{z,base}$ ($W$) is the power at the ground level.

#### 2.3.1. Numerical solutions of the WFE model based on finite difference method

The numerical solution (finite difference method) is preferred for the ease of realizing the approximate solution of the linear wind flow models in Eq. (10a) and percentage solar power gain in Eq. (10b). The linear equations are composed of differential and nondifferential linear terms. The solution is achieved by discretizing the differential and nondifferential linear terms.

#### 2.3.2. Space discretization of nondifferential linear terms

The discretization of the nondifferential linear terms is shown in Eq. (11)

$$u_z=u_{z,i}^n \tag{11}$$

#### 2.3.3. Space discretization of differential linear terms

The implicit and explicit discretization of the differential linear terms are based on their order (first and second) shown in Eqs. (12) and (13) respectively. Center discretization applies at the interior nodes, whereas forward discretization applies at the boundary nodes

$$\begin{aligned}
&\frac{\partial u_z}{\partial x}=\theta\frac{u_{z,i+1}^{n+1}-u_{z,i-1}^{n+1}}{2\Delta x}+(1-\theta)\frac{u_{z,i+1}^{n}-u_{z,i-1}^{n}}{2\Delta x};\\
&\frac{\partial u_z}{\partial y}=\theta\frac{u_{z,i+1}^{n+1}-u_{z,i-1}^{n+1}}{2\Delta y}+(1-\theta)\frac{u_{z,i+1}^{n}-u_{z,i-1}^{n}}{2\Delta y}
\end{aligned} \tag{12}$$

and

$$\begin{aligned}
&\frac{\partial^2 u_z}{\partial x^2}=\theta\frac{u_{z,i+1}^{n+1}-2u_{z,i}^{n+1}+u_{z,i-1}^{n+1}}{(\Delta x)^2}+(1-\theta)\frac{u_{z,i+1}^{n}-2u_{z,i}^{n}+u_{z,i-1}^{n}}{(\Delta x)^2};\\
&\frac{\partial^2 u_z}{\partial y^2}=\theta\frac{u_{z,i+1}^{n+1}-2u_{z,i}^{n+1}+u_{z,i-1}^{n+1}}{(\Delta y)^2}+(1-\theta)\frac{u_{z,i+1}^{n}-2u_{z,i}^{n}+u_{z,i-1}^{n}}{(\Delta y)^2}
\end{aligned} \tag{13}$$

where $\theta$ is the degree of implicitness, the superscript, $n$ denotes future time, whereas the subscript $i$ denotes the discretized nodes.

Substituting Eqs. (11), (12), (13) into Eq. (9) gives the discretized form of the WFE (GF $\neq$ 0, PGF $\neq$ 0) in the $z$-direction in Eq. (14)

$$\begin{aligned}
&-\left(\theta\left(u_{z,i+1}^{n+1}-u_{z,i-1}^{n+1}\right)+(1-\theta)\left(u_{z,i+1}^{n}-u_{z,i-1}^{n}\right)\right)\\
&-\left(\theta\left(u_{z,i+1}^{n+1}-u_{z,i-1}^{n+1}\right)+(1-\theta)\left(u_{z,i+1}^{n}-u_{z,i-1}^{n}\right)\right)\\
&=2\frac{\Delta z g_{z,i}}{u_{z,i}^n}-\frac{\Delta z u_{z,i}^n}{z_i^n}\\
&+2\left(\begin{aligned}
&\frac{\upsilon\Delta z}{u_{z,i}^n(\Delta x)^2}\left(\theta\left(u_{z,i+1}^{n+1}-2u_{z,i}^{n+1}+u_{z,i-1}^{n+1}\right)\right.\\
&\left.+(1-\theta)\left(u_{z,i+1}^{n}-2u_{z,i}^{n}+u_{z,i-1}^{n}\right)\right)\\
&+\frac{\upsilon\Delta z}{u_{z,i}^n(\Delta y)^2}\left(\theta\left(u_{z,i+1}^{n+1}-2u_{z,i}^{n+1}+u_{z,i-1}^{n+1}\right)\right.\\
&\left.+(1-\theta)\left(u_{z,i+1}^{n}-2u_{z,i}^{n}+u_{z,i-1}^{n}\right)\right)
\end{aligned}\right)\ \ \exists\ \ \upsilon=\frac{\mu}{\rho}
\end{aligned} \tag{14}$$

#### 2.3.4. Simplification of numerical solution of the WFE

The WFE, Eq. (14) is rearranged according to its implicit and explicit terms in Eq. (15)

$$\begin{aligned}
&2\theta\left(1-\xi_{x,z,i}^n-\xi_{y,z,i}^n\right)u_{z,i-1}^{n+1}+4\theta\left(\xi_{x,z,i}^n+\xi_{y,z,i}^n\right)u_{z,i}^{n+1}\\
&-2\theta\left(1+\xi_{x,z,i}^n+\xi_{y,z,i}^n\right)u_{z,i+1}^{n+1}=2\frac{(\Delta z)\,g_{z,i}}{u_{z,i}^n}-\frac{(\Delta z)\,u_{z,i}^n}{z_i^n}
\end{aligned}$$

$$+2\begin{pmatrix}\xi^n_{x,z,i}(1-\theta)\left(u^n_{z,i+1}-2u^n_{z,i}+u^n_{z,i-1}\right)\\+\xi^n_{y,z,i}(1-\theta)\left(u^n_{z,i+1}-2u^n_{z,i}+u^n_{z,i-1}\right)\end{pmatrix}$$
$$+2(1-\theta)\left(u^n_{z,i+1}-u^n_{z,i-1}\right)\quad\exists\quad\upsilon=\frac{\mu}{\rho},\ \xi^n_{x,z,i}=\frac{\upsilon\Delta z}{u^n_{z,i}(\Delta x)^2},$$
$$\xi^n_{y,z,i}=\frac{\upsilon\Delta z}{u^n_{z,i}(\Delta y)^2}$$
$$\textit{if }(\Delta x>\Delta y),\quad\xi^n_{x,z,i}<\xi^n_{y,z,i};\quad\textit{if }(\Delta x=\Delta y),$$
$$\xi^n_{x,z,i}=\xi^n_{y,z,i};\quad\textit{if }(\Delta x<\Delta y),\quad\xi^n_{x,z,i}>\xi^n_{y,z,i};\quad RHS^n_i\equiv f^n_{z,i}\tag{15}$$

where $\xi^n_{x,z,i}$ is the stability criterion in the (x-z)-direction and $\xi^n_{y,z,i}$ is the stability criterion in the (y-z)-direction, $RHS^n_i$ designates right hand side of the Eq. (15).

Considering $n=0$, $1\le i\le N-1$ leads to a diagonal matrix in Eq. (16a)–(16g)

$$4\theta\left(\xi^0_{x,z,1}+\xi^0_{y,z,1}\right)u^1_{z,1}-2\theta\left(1+\xi^0_{x,z,1}+\xi^0_{y,z,1}\right)u^1_{z,2}$$
$$=2\frac{(\Delta z)g_{z,1}}{u^0_{z,1}}-\frac{(\Delta z)u^0_{z,1}}{z^0_1}-2\theta\left(1-\xi^0_{x,z,1}-\xi^0_{y,z,1}\right)u^1_{z,0}$$
$$+2\begin{pmatrix}\xi^0_{x,z,1}(1-\theta)\left(u^0_{z,2}-2u^0_{z,1}+u^0_{z,0}\right)\\+\xi^0_{y,z,1}(1-\theta)\left(u^0_{z,2}-2u^0_{z,1}+u^0_{z,0}\right)\end{pmatrix}$$
$$+2(1-\theta)\left(u^0_{z,2}-u^0_{z,0}\right)\quad\exists\quad\upsilon=\frac{\mu}{\rho},\tag{16a}$$
$$\xi^0_{x,z,1}=\frac{\upsilon\Delta z}{u^0_{z,1}(\Delta x)^2},\ \xi^0_{y,z,1}=\frac{\upsilon\Delta z}{u^0_{z,1}(\Delta y)^2},$$
$$\textit{if }(\Delta x>\Delta y),\quad\xi_{x,z,1}<\xi_{y,z,1};\quad\textit{if }(\Delta x=\Delta y),$$
$$\xi_{x,z,1}=\xi_{y,z,1};\quad\textit{if }(\Delta x<\Delta y),\quad\xi_{x,z,1}>\xi_{y,z,1};\quad RHS^0_{z,1}\equiv f^0_{z,1}$$
$$u^0_{z,0}=2u^0_{z,1}-u^0_{z,2},\ \ u^1_{z,0}-u^0_{z,0}\approx\Delta z\,G,\ \ \Delta z\,(m)\ ,\ G\left(\frac{\text{m/s}}{m}\right)$$

$$2\theta\left(1-\xi^0_{x,z,2}-\xi^0_{y,z,2}\right)u^1_{z,1}+4\theta\left(\xi^0_{x,z,2}+\xi^0_{y,z,2}\right)u^1_{z,2}$$
$$-2\theta\left(1+\xi^0_{x,z,2}+\xi^0_{y,z,2}\right)u^1_{z,3}=2\frac{(\Delta z)g_{z,2}}{u^0_{z,2}}-\frac{(\Delta z)u^0_{z,2}}{z^0_2}$$
$$+2\begin{pmatrix}\xi^0_{x,z,2}(1-\theta)\left(u^0_{z,3}-2u^0_{z,2}+u^0_{z,1}\right)\\+\xi^0_{y,z,2}(1-\theta)\left(u^0_{z,3}-2u^0_{z,2}+u^0_{z,1}\right)\end{pmatrix}$$
$$+2(1-\theta)\left(u^0_{z,3}-u^0_{z,1}\right)\quad\exists\quad\upsilon=\frac{\mu}{\rho},\tag{16b}$$
$$\xi^0_{x,z,2}=\frac{\upsilon\Delta z}{u^0_{z,2}(\Delta x)^2},\ \xi^0_{y,z,2}=\frac{\upsilon\Delta z}{u^0_{z,2}(\Delta y)^2},$$
$$\textit{if }(\Delta x>\Delta y),\quad\xi_{x,z,2}<\xi_{y,z,2};\quad\textit{if }(\Delta x=\Delta y),$$
$$\xi_{x,z,2}=\xi_{y,z,2};\quad\textit{if }(\Delta x<\Delta y),\quad\xi_{x,z,2}>\xi_{y,z,2};\quad RHS^0_{z,2}\equiv f^0_{z,2}$$

$$2\theta\left(1-\xi^0_{x,z,3}-\xi^0_{y,z,3}\right)u^1_{z,2}+4\theta\left(\xi^0_{x,z,3}+\xi^0_{y,z,3}\right)u^1_{z,3}$$
$$-2\theta\left(1+\xi^0_{x,z,3}+\xi^0_{y,z,3}\right)u^1_{z,4}$$
$$=2\frac{(\Delta z)g_{z,3}}{u^0_{z,3}}-\frac{(\Delta z)u^0_{z,3}}{z^0_3}$$
$$+2\begin{pmatrix}\xi^0_{x,z,3}(1-\theta)\left(u^0_{z,4}-2u^0_{z,3}+u^0_{z,2}\right)\\+\xi^0_{y,z,3}(1-\theta)\left(u^0_{z,4}-2u^0_{z,3}+u^0_{z,2}\right)\end{pmatrix}$$
$$+2(1-\theta)\left(u^0_{z,4}-u^0_{z,2}\right)\quad\exists\quad\upsilon=\frac{\mu}{\rho},\ \xi^0_{x,z,3}=\frac{\upsilon\Delta z}{u^0_{z,3}(\Delta x)^2},\tag{16c}$$
$$\xi^0_{y,z,3}=\frac{\upsilon\Delta z}{u^0_{z,3}(\Delta y)^2},$$
$$\textit{if }(\Delta x>\Delta y),\quad\xi_{x,z,3}<\xi_{y,z,3};\quad\textit{if }(\Delta x=\Delta y),$$
$$\xi_{x,z,3}=\xi_{y,z,3};\quad\textit{if }(\Delta x<\Delta y),\quad\xi_{x,z,3}>\xi_{y,z,3};\quad RHS^0_{z,3}\equiv f^0_{z,3}$$

$$\vdots\tag{16d}$$

$$2\theta\left(1-\xi^0_{x,z,N-3}-\xi^0_{y,z,N-3}\right)u^1_{z,N-4}+4\theta\left(\xi^0_{x,z,N-3}+\xi^0_{y,z,N-3}\right)u^1_{z,N-3}$$
$$-2\theta\left(1+\xi^0_{x,z,N-3}+\xi^0_{y,z,N-3}\right)u^1_{z,N-2}$$
$$=2\frac{(\Delta z)g_{z,N-3}}{u^0_{z,N-3}}-\frac{(\Delta z)u^0_{z,N-3}}{z^0_{N-3}}$$
$$+2\begin{pmatrix}\xi^0_{x,z,N-3}(1-\theta)\left(u^0_{z,N-4}-2u^0_{z,N-3}+u^0_{z,N-2}\right)\\+\xi^0_{y,z,N-3}(1-\theta)\left(u^0_{z,N-4}-2u^0_{z,N-3}+u^0_{z,N-2}\right)\end{pmatrix}$$
$$+2(1-\theta)\left(u^0_{z,N-2}-u^0_{z,N-4}\right)\quad\exists\quad\upsilon=\frac{\mu}{\rho},\ \xi^0_{x,z,N-3}=\frac{\upsilon\Delta z}{u^0_{z,N-3}(\Delta x)^2},$$
$$\xi^0_{y,z,N-3}=\frac{\upsilon\Delta z}{u^0_{z,N-3}(\Delta y)^2},$$
$$\textit{if }(\Delta x>\Delta y),\quad\xi_{x,z,N-3}<\xi_{y,z,N-3};\quad\textit{if }(\Delta x=\Delta y),$$
$$\xi_{x,z,N-3}=\xi_{y,z,N-3};\quad\textit{if }(\Delta x<\Delta y),\quad\xi_{x,z,N-3}>\xi_{y,z,N-3};$$
$$RHS^0_{z,N-3}\equiv f^0_{z,N-3}\tag{16e}$$

$$2\theta\left(1-\xi^0_{x,z,N-2}-\xi^0_{y,z,N-2}\right)u^1_{z,N-3}+4\theta\left(\xi^0_{x,z,N-2}+\xi^0_{y,z,N-2}\right)u^1_{z,N-2}$$
$$-2\theta\left(1+\xi^0_{x,z,N-2}+\xi^0_{y,z,N-2}\right)u^1_{z,N-1}=2\frac{(\Delta z)g_{z,N-2}}{u^0_{z,N-2}}-\frac{(\Delta z)u^0_{z,N-2}}{z^0_{N-2}}$$
$$+2\begin{pmatrix}\xi^0_{x,z,N-2}(1-\theta)\left(u^0_{z,N-3}-2u^0_{z,N-2}+u^0_{z,N-1}\right)\\+\xi^0_{y,z,N-2}(1-\theta)\left(u^0_{z,N-3}-2u^0_{z,N-2}+u^0_{z,N-1}\right)\end{pmatrix}$$
$$+2(1-\theta)\left(u^0_{z,N-1}-u^0_{z,N-3}\right)\quad\exists\quad\upsilon=\frac{\mu}{\rho},\ \xi^0_{x,z,N-2}=\frac{\upsilon\Delta z}{u^0_{z,N-2}(\Delta x)^2},$$
$$\xi^0_{y,z,N-2}=\frac{\upsilon\Delta z}{u^0_{z,N-2}(\Delta y)^2},$$
$$\textit{if }(\Delta x>\Delta y),\quad\xi_{x,z,N-2}<\xi_{y,z,N-2};\quad\textit{if }(\Delta x=\Delta y),$$
$$\xi_{x,z,N-2}=\xi_{y,z,N-2};\quad\textit{if }(\Delta x<\Delta y),\quad\xi_{x,z,N-2}>\xi_{y,z,N-2};$$
$$RHS^0_{z,N-2}\equiv f^0_{z,N-2}\tag{16f}$$

$$2\theta\left(1-\xi^0_{x,z,N-1}-\xi^0_{y,z,N-1}\right)u^1_{z,N-2}+4\theta\left(\xi^0_{x,z,N-1}+\xi^0_{y,z,N-1}\right)u^1_{z,N-1}$$
$$=2\frac{(\Delta z)g_{z,N-1}}{u^0_{z,N-1}}-\frac{(\Delta z)u^0_{z,N-1}}{z^0_{N-1}}+2\theta\left(1+\xi^0_{x,z,N-1}+\xi^0_{y,z,N-1}\right)u^1_{z,N}$$
$$+2\begin{pmatrix}\xi^0_{x,z,N-1}(1-\theta)\left(u^0_{z,N-2}-2u^0_{z,N-1}+u^0_{z,N}\right)\\+\xi^0_{y,z,N-1}(1-\theta)\left(u^0_{z,N-2}-2u^0_{z,N-1}+u^0_{z,N}\right)\end{pmatrix}$$
$$+2(1-\theta)\left(u^0_{z,N}-u^0_{z,N-2}\right)\quad\exists\quad\upsilon=\frac{\mu}{\rho},\ \xi^0_{x,z,N-1}=\frac{\upsilon\Delta z}{u^0_{z,N-1}(\Delta x)^2},$$
$$\xi^0_{y,z,N-1}=\frac{\upsilon\Delta z}{u^0_{z,N-1}(\Delta y)^2},$$
$$\textit{if }(\Delta x>\Delta y),\quad\xi_{x,z,N-1}<\xi_{y,z,N-1};\quad\textit{if }(\Delta x=\Delta y),$$
$$\xi_{x,z,N-1}=\xi_{y,z,N-1};\quad\textit{if }(\Delta x<\Delta y),\quad\xi_{x,z,N-1}>\xi_{y,z,N-1};$$
$$RHS^0_{z,N-1}\equiv f^0_{z,N-1}$$
$$u^0_{z,N}=2u^0_{z,N-1}-u^0_{z,N-2},\quad u^1_{z,N}-u^0_{z,N}\approx\Delta z\,G,$$
$$\Delta z\,(m)\ ,\ G\left(\frac{\text{m/s}}{m}\right)\tag{16g}$$

where $N$ is the mesh size ($N=111$ is used in the numerical computation).

The tridiagonal matrix notation of Eqs. (16a)–(16g), WFE in $z$-direction is given in Eq. (17a) , that is given in Box I.

Similarly, the tridiagonal matrix of the percentage power gain, $p_z$ (%) is given in Eq. (17b), that is given in Box II.

where $g^0_{z,i}\equiv f^0_{z,i}$.

$$\begin{bmatrix} 4\theta\left(\xi_{x,z,1}+\xi_{y,z,1}\right) & -2\theta\left(1+\xi_{x,z,1}+\xi_{y,z,1}\right) & 0 & 0 & 0 \\ 2\theta\left(1-\xi_{x,z,2}-\xi_{y,z,2}\right) & 4\theta\left(\xi_{x,z,2}+\xi_{y,z,2}\right) & \ddots & 0 & 0 \\ 0 & 2\theta\left(1-\xi_{x,z,3}-\xi_{y,z,3}\right) & \ddots & -2\theta\left(1+\xi_{x,z,N-3}+\xi_{y,z,N-3}\right) & 0 \\ 0 & 0 & \ddots & 4\theta\left(\xi_{x,z,N-2}+\xi_{y,z,N-2}\right) & -2\theta\left(1+\xi_{x,z,N-2}+\xi_{y,z,N-2}\right) \\ 0 & 0 & 0 & 2\theta\left(1-\xi_{x,z,N-1}-\xi_{y,z,N-1}\right) & 4\theta\left(\xi_{x,z,N-1}+\xi_{y,z,N-1}\right) \end{bmatrix}\begin{bmatrix} u^1_{Z,1} \\ u^1_{Z,2} \\ \vdots \\ u^1_{Z,N-2} \\ u^1_{Z,N-1} \end{bmatrix} = \begin{bmatrix} f^0_{z,1} \\ f^0_{z,2} \\ \vdots \\ f^0_{z,N-2} \\ f^0_{z,N-1} \end{bmatrix} \tag{17a}$$

**Box I.**

$$\begin{bmatrix} 4\theta\left(\xi_{x,z,1}+\xi_{y,z,1}\right) & -2\theta\left(1+\xi_{x,z,1}+\xi_{y,z,1}\right) & 0 & 0 & 0 \\ 2\theta\left(1-\xi_{x,z,2}-\xi_{y,z,2}\right) & 4\theta\left(\xi_{x,z,2}+\xi_{y,z,2}\right) & \ddots & 0 & 0 \\ 0 & 2\theta\left(1-\xi_{x,z,3}-\xi_{y,z,3}\right) & \ddots & -2\theta\left(1+\xi_{x,z,N-3}+\xi_{y,z,N-3}\right) & 0 \\ 0 & 0 & \ddots & 4\theta\left(\xi_{x,z,N-2}+\xi_{y,z,N-2}\right) & -2\theta\left(1+\xi_{x,z,N-2}+\xi_{y,z,N-2}\right) \\ 0 & 0 & 0 & 2\theta\left(1-\xi_{x,z,N-1}-\xi_{y,z,N-1}\right) & 4\theta\left(\xi_{x,z,N-1}+\xi_{y,z,N-1}\right) \end{bmatrix}\begin{bmatrix} p^1_{Z,1} \\ p^1_{Z,2} \\ \vdots \\ p^1_{Z,N-2} \\ p^1_{Z,N-1} \end{bmatrix} = \begin{bmatrix} g^0_{z,1} \\ g^0_{z,2} \\ \vdots \\ g^0_{z,N-2} \\ g^0_{z,N-1} \end{bmatrix} \tag{17b}$$

**Box II.**

The kinematic viscosity, $\upsilon(\mathrm{m}^2/\mathrm{s})$ is defined by Nnamchi et al. (2019) in Eq. (18) as

$$\upsilon = \frac{1.03\times10^{-06}+7.0\times10^{-08}T_z-4\times10^{-11}T_z^2}{2.1313-0.003T_z} \quad \exists \quad T\,(K) \tag{18}$$

Temperature variation from the surface to the top of the troposphere, $T_z$ (K) is defined in Eq. (19) according to https://www.weather.gov/jetstream/laye data

$$T_z = T_{surface} + \frac{\left(T_{top}-T_{surface}\right)\left(h_z-h_{surface}\right)}{\left(h_{top}-h_{surface}\right)} \quad \exists \quad T\ (\mathrm{K}),\quad h\,(\mathrm{m}),$$
$$T_{top} = 222.15\ \mathrm{K},\ T_{surface} = 290.15\ \mathrm{K},$$
$$h_{top} = 18000\ \mathrm{m},\quad h_{surface} = 0.0\ \mathrm{m},\quad h_z = h_{Altitude} - h_{Elevation} \tag{19}$$

where $T$ (K) is the temperature, $h$ (m) is the height above ground level.

Validation of tropospheric wind speed ($u_z$) is based on statistical tool, root mean square error, RMSE in Eq. (20)

$$RMSE_{u_{zz}} = \sqrt{\frac{\sum\left(u_{z,simul}-\bar{u}_{z,radiosonde}\right)^2}{N}} \tag{20}$$

Validation of near surface percentage solar power gain (p) is based on statistical tool, root mean square error, RMSE in Eq. (21)

$$RMSE_{P_z} = \sqrt{\frac{\sum\left(p_{z,simul}-p_{z,measured}\right)^2}{N}} \tag{21}$$

where $N$ is the number of data observed.

*2.3.5. Solution techniques, simulation procedure and the convergence criterion*

Numerical solutions of the differential models in Eqs. (1a), (1b), (1a), (2b), (4) are sort by finite difference scheme using Crank Nicolson technique (with degree of implicitness, $\psi = 0.5$) with mesh size of 111. The boundary and center nodes were

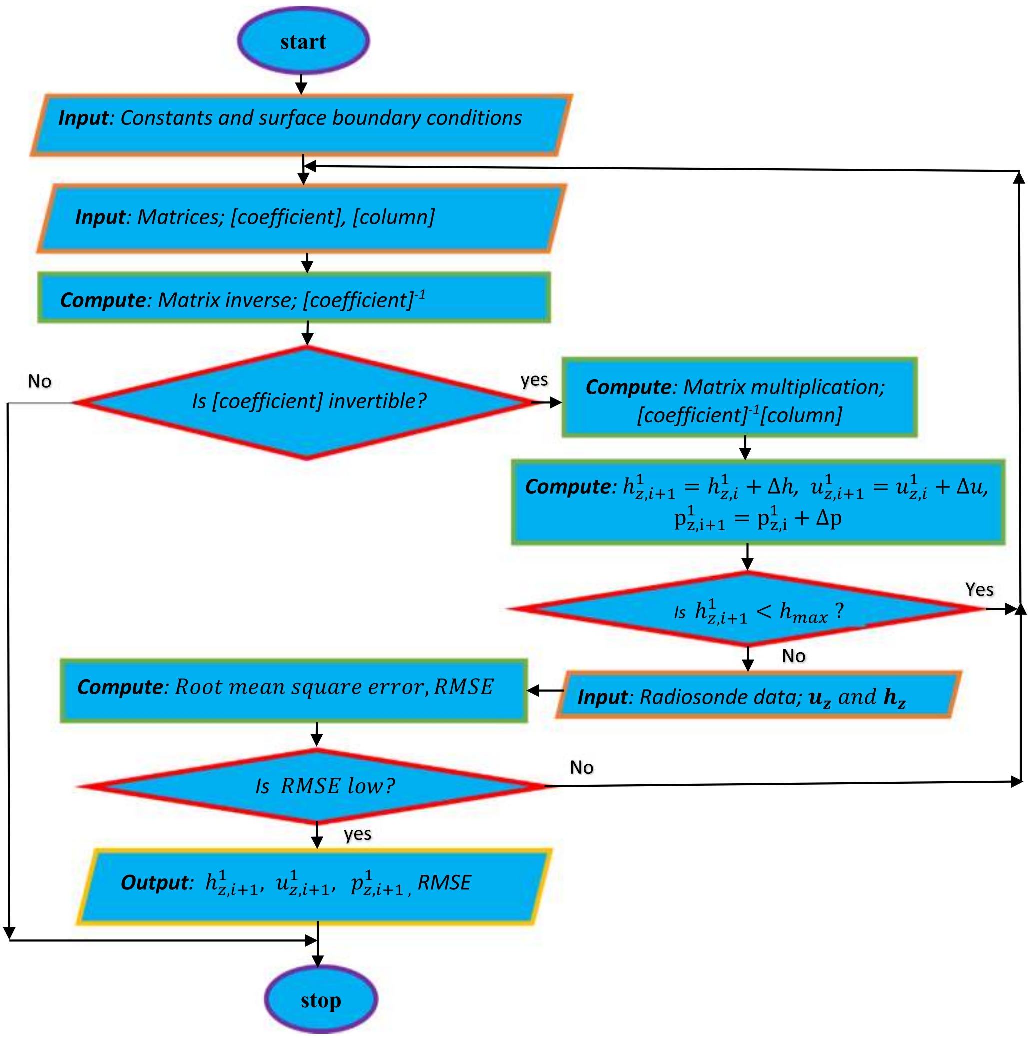


**Fig. 4.** Flowchart for determining percentage of solar power gain.

discretized with forward and center discretization, respectively. Eqs. (7), (8), (9) are steady flow equations, thus, First-kind or Dirichlet boundary conditions apply in the development of wind speed flow field and percentage power gain distribution (the boundary conditions are potentials). At tropospheric height of zero (ground surface), the wind speed and percentage power gain were considered to be zero.

Vitally, the pressure term in Eqs. (1a), (1b), (1c), (1a), (2b), (3c) was approximated as a product of air density and square of the wind velocity ($P \approx 0.5\rho u^2$) to maintain wind speed as a lone dependent variable and for the ease of the solution. In addition, the continuity equation was useful in developing an approximate relation among the component wind velocities with respect to their step change. This further simplified the model and made it amenable to solution as only one potential is left in the component wind velocity models in Eqs. (7), (8), (9). The input data for the simulation are basically, the boundary potentials and constants found in the numerical equations (Eq. (15)). The tridiagonal matrices in Eqs. (17a) and (17b) were used to calculate the future potential. The simulation was terminated as tropospheric height equalizes with the first circling tropospheric height ($h_z = 9200$ m). The flow chart illustrating the model solution and simulation procedure is presented in Fig. 4. The algorithm is made of input data to the tridiagonal matrix, computes the new set of model potentials, and outputs future model potentials with the corresponding tropospheric heights and wind speed.

## 3. Results and discussion

### 3.1. Results

The results are presented in both tables and figures. Table 1 shows wind speed boundary conditions at ground level for Eq. (17a) and Eq. (17b), defining the wind speed and percentage of solar power gain at ground level (depressed station, tropospheric height is zero). Tables 2–4 present the solar power measured results for the elevated (above ground level) station 1 (Engineering Complex), station 2 (Hostel Complex) and station 3 (Library Complex), respectively. In addition, Tables 2–4 present the solar power measured results for the depressed (ground level) station 1 (Engineering Complex), station 2 (Hostel Complex) and station 3 (Library Complex), respectively. Table 5 portrays statistical validation of tropospheric wind speed and percentage solar power gain based on root mean square error, RMSE in Eqs. (20) and (21). The simulation of the percentage of solar power gain was limited to an altitude of 9200 m with a corresponding wind speed of 42 m/s. The tropospheric height is the difference between the altitude and the elevation of the study areas. Toward the second circling in the radiosonde (Fig. 1), the wind speed decreased drastically to zero before rising again. Thus, the altitudes with decreasing to zero wind speed were neglected in this analysis as the effect of wind speed diminished and later vanished.

**Table 1**
Surface wind flow and percentage power gain boundary conditions for the study areas.

| Study area | Dimension (km) | Wind speed boundary condition (m/s) | Percentage power gain boundary condition (–) |
|---|---|---|---|
| NR | $(x \neq 0, y \neq 0, z = 0)$ | $u_x = u_y = u_z = 0$ | $p_z = 0$ |
| ER | $(x \neq 0, y \neq 0, z = 0)$ | $u_x = u_y = u_z = 0$ | $p_z = 0$ |
| CR | $(x \neq 0, y \neq 0, z = 0)$ | $u_x = u_y = u_z = 0$ | $p_z = 0$ |
| WR | $(x \neq 0, y \neq 0, z = 0)$ | $u_x = u_y = u_z = 0$ | $p_z = 0$ |

**Table 2**
Measured average data at station 1 (Engineering Complex at Kampala International University, WC).

| Parameter | Local time (pm) | | | | | | | | | |
|---|---|---|---|---|---|---|---|---|---|---|
| | Elevated station | | | | | Depressed or ground station | | | | |
| | 1:00 | 1:15 | 1:30 | 1:45 | 2:00 | 1:00 | 1:15 | 1:30 | 1:45 | 2:00 |
| Tropospheric height, $h_z$ (m) | 19.26 | 19.26 | 19.26 | 19.26 | 19.26 | 0 | 0 | 0 | 0 | 0 |
| Wind speed, $u_z$ (m/s) | 2.50 | 2.64 | 2.68 | 2.54 | 2.66 | 0 | 0 | 0 | 0 | 0 |
| Short circuit current, $I$ (A) | 0.24 | 0.53 | 0.56 | 0.58 | 0.58 | 0.23 | 0.51 | 0.54 | 0.56 | 0.56 |
| Open circuit voltage, $V$ (V) | 21 | 21 | 21 | 21 | 21 | 21 | 21 | 21 | 21 | 21 |
| Measured power, $P_z$ (W) | 4.94 | 11.13 | 11.76 | 12.18 | 12.18 | 4.75 | 10.72 | 11.32 | 11.74 | 11.73 |
| Measured percentage power gain, $p_{measured}$ (%) | 0.038 | 0.038 | 0.039 | 0.038 | 0.038 | 0 | 0 | 0 | 0 | 0 |
| Simulated percentage power gain, $p_{simulated}$ (% | 0.043 | 0.045 | 0.046 | 0.044 | 0.046 | 0 | 0 | 0 | 0 | 0 |

**Table 3**
Measured average data at station 2 (Hostel Complex of Kampala International University, WC).

| Parameter | Local time (pm) | | | | | | | | | |
|---|---|---|---|---|---|---|---|---|---|---|
| | Elevated station | | | | | Depressed or ground station | | | | |
| | 1:00 | 1:15 | 1:30 | 1:45 | 2:00 | 1:00 | 1:15 | 1:30 | 1:45 | 2:00 |
| Tropospheric height, $h_z$ (m) | 37.65 | 37.65 | 37.65 | 37.65 | 37.65 | 0 | 0 | 0 | 0 | 0 |
| Wind speed, $u_z$ (m/s) | 2.66 | 2.64 | 2.79 | 2.63 | 2.60 | 0 | 0 | 0 | 0 | 0 |
| Short circuit current, $I$ (A) | 0.34 | 0.37 | 0.44 | 0.50 | 0.53 | 0.32 | 0.35 | 0.38 | 0.48 | 0.49 |
| Open circuit voltage, $V$ (V) | 20.27 | 21.80 | 20.00 | 20.72 | 20.05 | 20.11 | 21.69 | 21.51 | 20.61 | 20.18 |
| Measured power, $P_z$ (W) | 6.95 | 8.10 | 8.70 | 10.45 | 10.65 | 6.48 | 7.59 | 8.17 | 9.89 | 9.89 |
| Measured percentage power gain, $p_{measured}$ (%) | 0.074 | 0.07 | 0.07 | 0.06 | 0.08 | 0 | 0 | 0 | 0 | 0 |
| Simulated percentage power gain, $p_{simulated}$ (%) | 0.086 | 0.077 | 0.110 | 0.066 | 0.100 | 0 | 0 | 0 | 0 | 0 |

**Table 4**
Measured average data at station 3 (Library Complex of Kampala International University, WC).

| Parameter | Local time (pm) | | | | | | | | | |
|---|---|---|---|---|---|---|---|---|---|---|
| | Elevated station | | | | | Depressed or ground station | | | | |
| | 1:00 | 1:15 | 1:30 | 1:45 | 2:00 | 1:00 | 1:15 | 1:30 | 1:45 | 2:00 |
| Tropospheric height, $h_z$ (m) | 77.7 | 77.7 | 77.7 | 77.7 | 77.7 | 0 | 0 | 0 | 0 | 0 |
| Wind speed, $u_z$ (m/s) | 2.69 | 2.75 | 2.67 | 2.75 | 2.74 | 0 | 0 | 0 | 0 | 0 |
| Short circuit current, $I$ (A) | 0.53 | 0.57 | 0.57 | 0.53 | 0.49 | 0.25 | 0.24 | 0.24 | 0.23 | 0.23 |
| Open circuit voltage, $V$ (V) | 22 | 21 | 20 | 21 | 22 | 21 | 21 | 21 | 21 | 21 |
| Measured power $P_z$ (–) | 11.56 | 11.78 | 11.48 | 11.22 | 10.75 | 10.08 | 10.33 | 9.98 | 9.84 | 9.42 |
| Measured percentage power gain $p_{simulated}$ (%) | 0.15 | 0.14 | 0.15 | 0.14 | 0.14 | 0 | 0 | 0 | 0 | 0 |
| Simulated percentage power gain $p_{simulated}$ (%) | 0.17 | 0.16 | 0.17 | 0.16 | 0.16 | 0 | 0 | 0 | 0 | 0 |

**Table 5**
Statistical validation of simulated results.

| Study area | Root mean square error, RMSE | | |
|---|---|---|---|
| | Tropospheric wind speed, $RMSE_{u_z}$ | Measurement location | Near surface percentage power gain, $RMSE_{p_z}$ |
| Northern Region, NR | 8.792 | Engineering complex | 0.010 |
| Eastern Region, ER | 8.789 | Hostel complex | 0.021 |
| Central Region, CR | 9.879 | Library complex | 0.020 |
| Western Region, WR | 9.447 | | |

Figs. 5–8 portray fitted line graph of troposphere Height against the wind speed for NR, ER, CR and WR, respectively. Similarly, Figs. 9–12 portray simple line graph of wind speed against the percentage of solar power gain for NR, ER, CR and WR, respectively. Whereas Figs. 13–16 give the composite or contour plot of the percentage of solar power gain against tropospheric Height and the wind speed. These results are germane for discussion and drawing apt conclusions

### 3.2. Discussion

The results are discussed according to the three cardinal objectives of the study; establishment of the functional relationship between the tropospheric height and the wind speed, formulation of the functional relationship between the tropospheric height and percentage of power gain, and lastly unification of the three

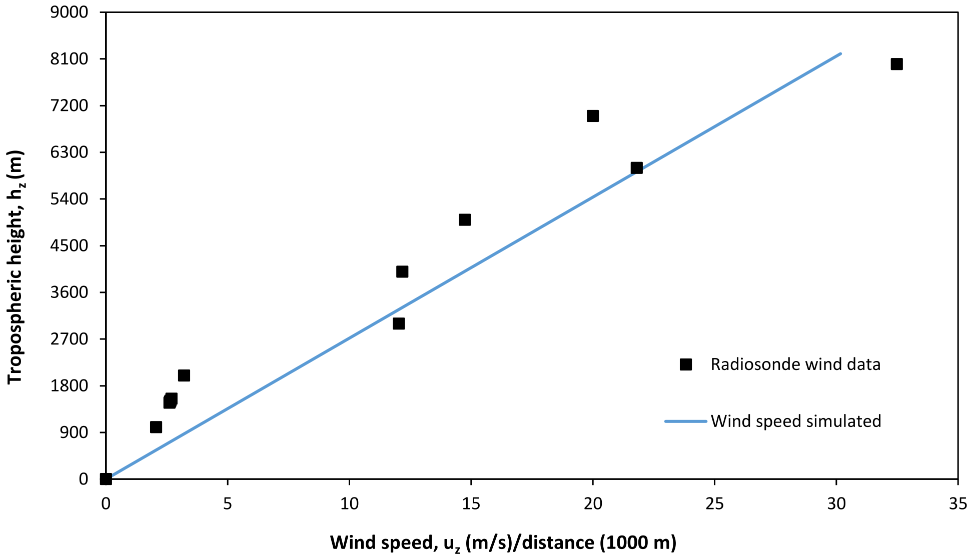


**Fig. 5.** Growth of tropospheric height with the wind speed for the Northern Region.

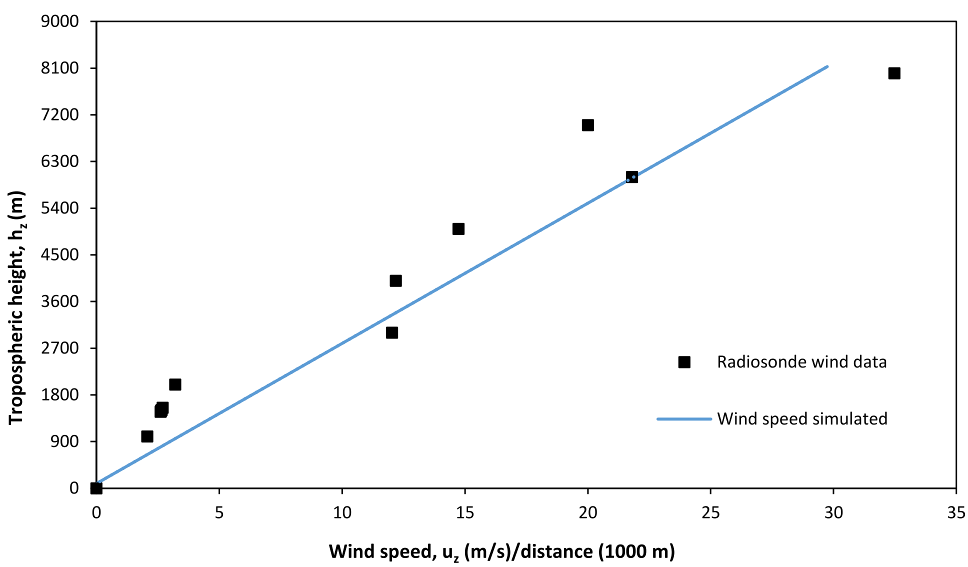


**Fig. 6.** Reliance of tropospheric height on the wind speed for the Eastern Region.

parameters (percentage of solar power gain, tropospheric Height and wind speed) in contour for the study areas.

*3.2.1. Functional relationship between tropospheric height and the wind speed*

Figs. 5, 6, 7, 8 demonstrate the linear behavior between the tropospheric height and the wind speed for the study area (Fig. 2). This result supports that Eq. (3a) is a linear partial derivative model of WFE because the body or external forces were not considered in their formulations, however, it describes the smooth linear relation between wind speed and tropospheric height. Despite the radiosonde data in Fig. 1 showed a wavy curve between the altitude and the wind speed. The tropospheric height is derived from the radiosonde by subtracting the elevation of the study areas from the altitude. The radiosonde measured data fairly fitted well with the simulated results in Figs. 5–8, the agreement supports the implementation of simulated results in this work with the aid of RMSE. The validity of simulated tropospheric wind velocity with the radiosonde results is supported by the moderate values of the RMSE for the regional study areas in Table 5 (NR, ER, CR. WR with corresponding RMSE of 7.792, 8.789, 9.879, 9.447, respectively). The root mean square error results for the Central, and Eastern Regions are higher than those of the Northern and Western Regions, showing that the dispersion between the simulated, and radiosonde data is pronounced in the Central and Eastern Regions relative to the Northern and Western Regions due variation in the topography. In addition, above the ground level, the influence of topography becomes insignificant, thus, the wind speed data in both north–south and east–west directions cluster as shown in Figs. 5–8. Significant wind speeds of approximately 33 and 42 $ms^{-1}$/distance 1000 m correspond to tropospheric heights of 8100 and 9200 m, respectively, these wind speeds are very good for wind farm operations provided a stack of these heights is available in the regions.

*3.2.2. Functional relationship between tropospheric height and percentage power gain*

Figs. 9–12 display the linear behavior between the percentage of solar power gain and the tropospheric height for the study areas in Fig. 2. Similarly, these results support that Eq. (10b)

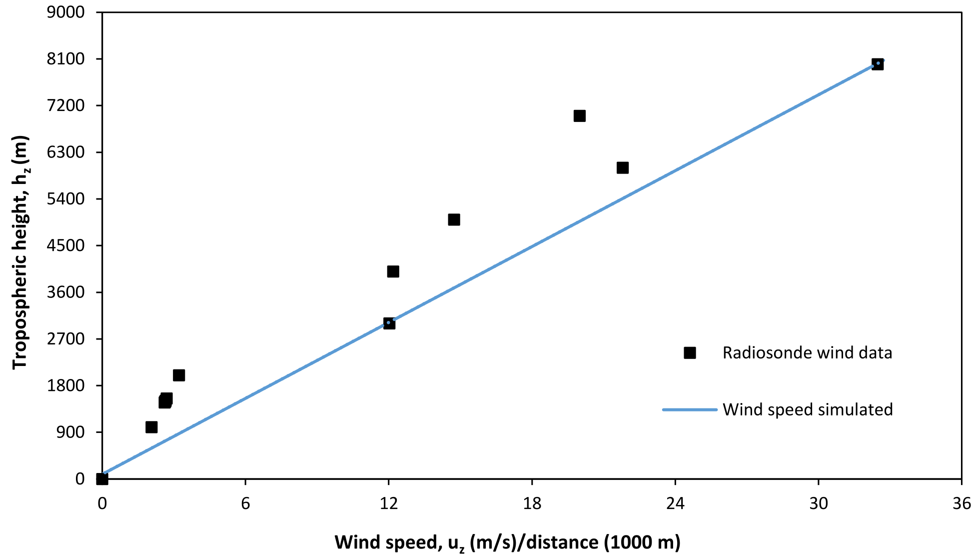


**Fig. 7.** Dependence of tropospheric height on the wind speed for the Central Region.

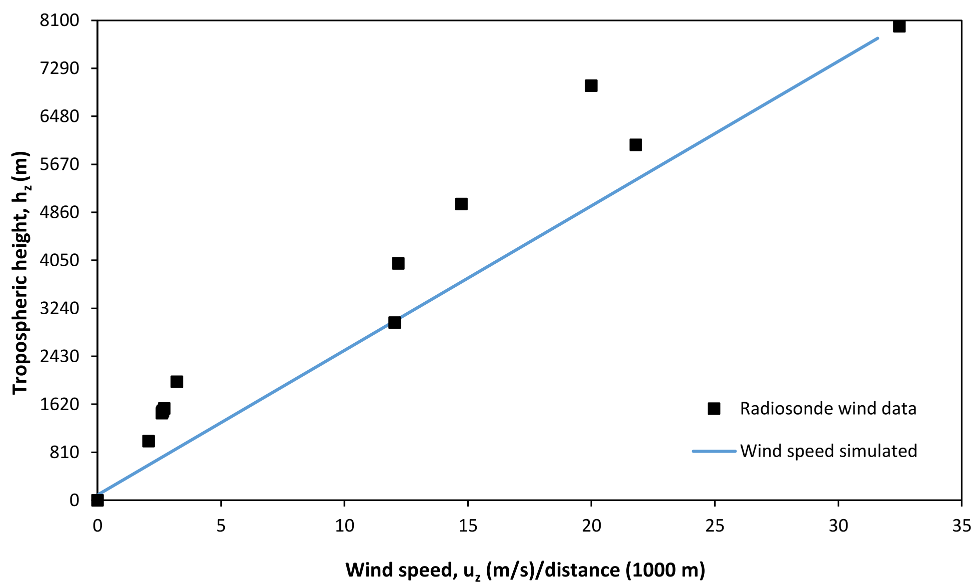


**Fig. 8.** Variation of tropospheric height with the wind speed for the Western Region.

is a linear partial derivative model of WFE because the body or external forces as earlier mentioned were not considered in their formulations, nevertheless, it defines the linear relationship between the percentage of solar power gain and tropospheric height. In addition, above the ground level, the influence of topography becomes unimportant, as the percentage of solar power gain in both north south and east west directions cluster as shown in Figs. 9–12. Figs. 9–12 could not be fitted because measurements could not be carried in the high tropospheric height. However, Tables 2–4 shows practical measurement of the percentage of solar power gain, the measurements are conducted close to ground level in three elevated stations in Figs. 3a, 3b, 3c. The root mean square error (RMSE) analysis of simulated and measured solar power results gave 0.010, 0.021, 0.020 in Table 5, respectively, thus, the low value of RMSE implies strong agreement between simulated and measured percentage solar power gain. The practical measurement supports that the higher the near ground height, the higher solar power is generated, thus, RMSE at the Engineering is less than the RMSE at Hostel, and Library complexes. The variation in RMSE could be attributed to changes in experimental conditions as the measurement were carried out on different days in different stations. Above the tropospheric height, of 9200 m, the wind speed diminished to zero, thus, a maximum tropospheric of 9200 m was considered in this work since wind speed is defined from ground level to this height (9200 m).

#### 3.2.3. Composite behavior of percentage of solar power gain with tropospheric height and wind speed

The percentage of solar power gain was simulated in space where both the tropospheric height and the wind speed are defined. The composite behavior of percentage of solar power gain yielded the contour plots in Figs. 13–16 for NR, ER, CR and WR, respectively. Remarkable the percentage of solar power gain isolines shows the range of tropospheric heights and wind velocity that support such percentage solar power gain. It obvious that from ground level to approximately 1000 m that small

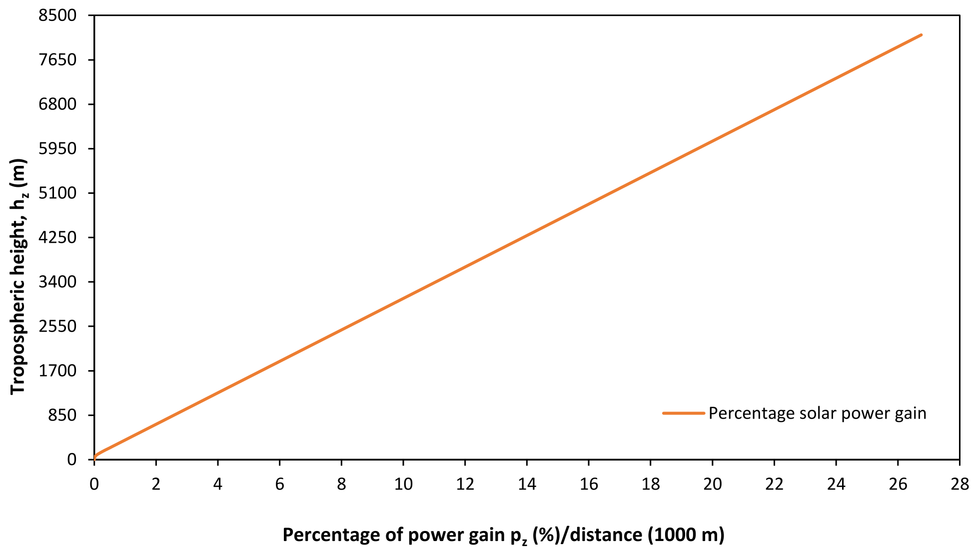


**Fig. 9.** Growth of tropospheric height with the percentage of solar power gain for the Northern Region.

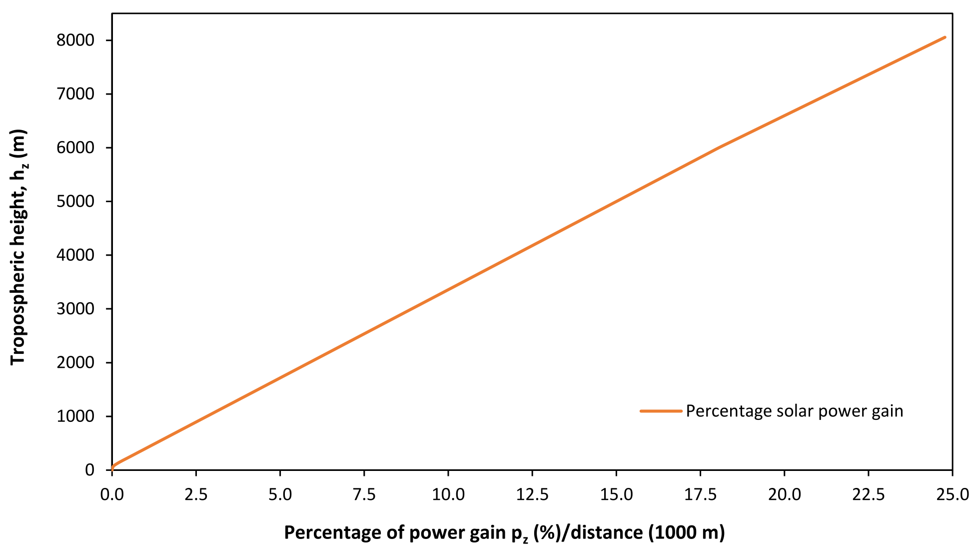


**Fig. 10.** Impact of tropospheric height on the percentage of solar power gain for the Eastern Region.

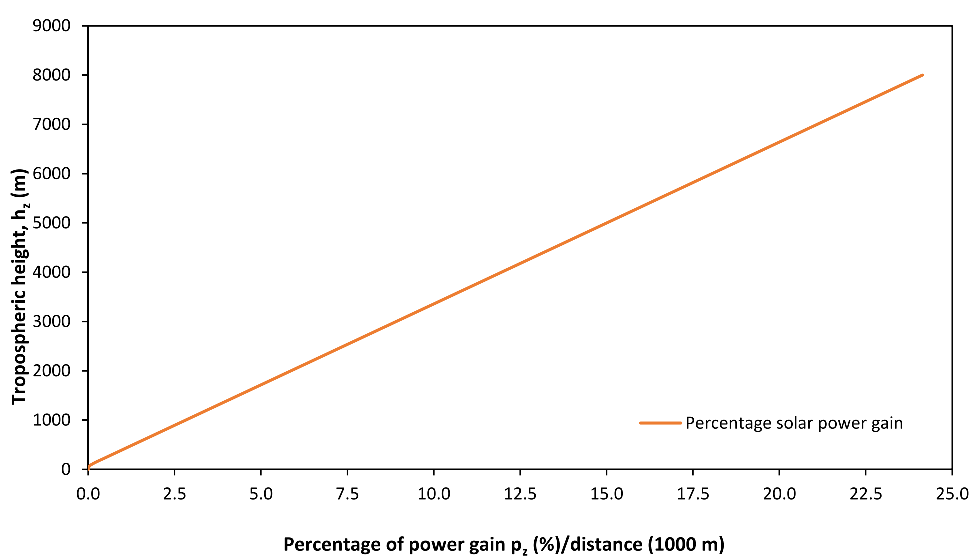


**Fig. 11.** Influence of tropospheric height on the percentage of solar power gain for the Central Region.

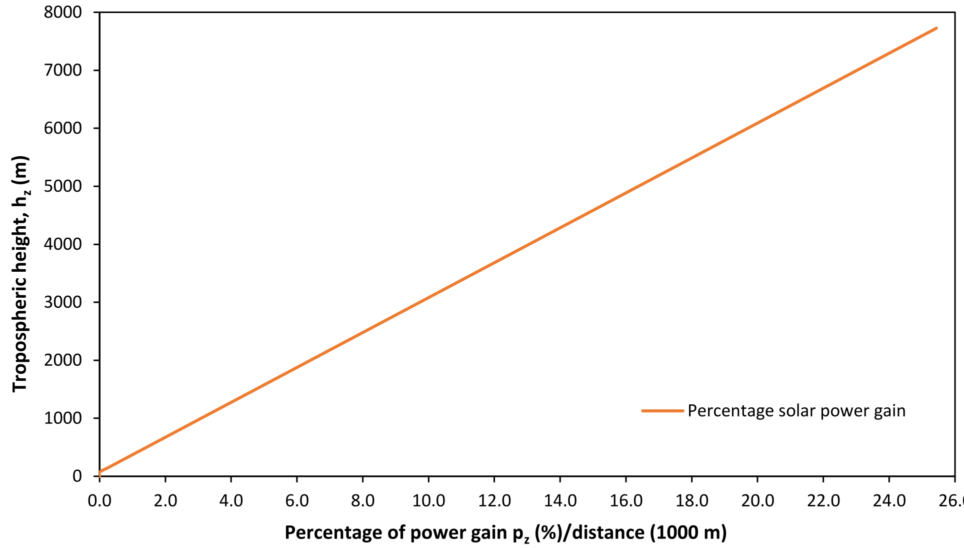


**Fig. 12.** Effect of tropospheric height on the percentage of solar power gain for the Western Region.

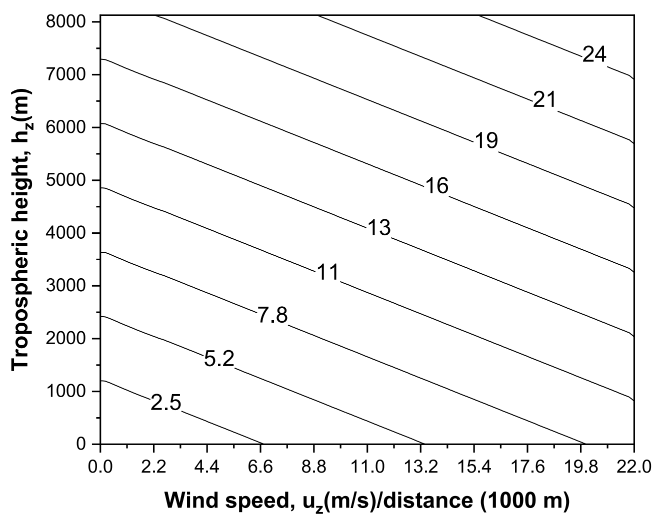


**Fig. 13.** Response of the percentage of solar power gain, $p_z$ (% ) to tropospheric height and wind speed for the Northern Region.

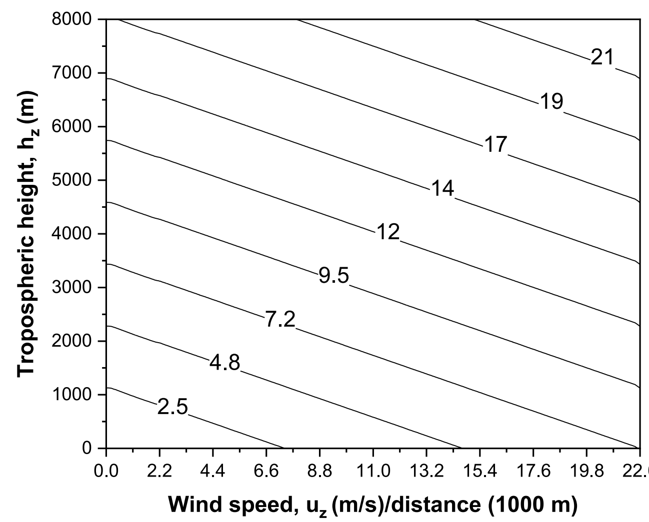


**Fig. 15.** Reaction of the percentage of solar power gain, $p_z$ (% ) to tropospheric height and wind speed for the Central Region.

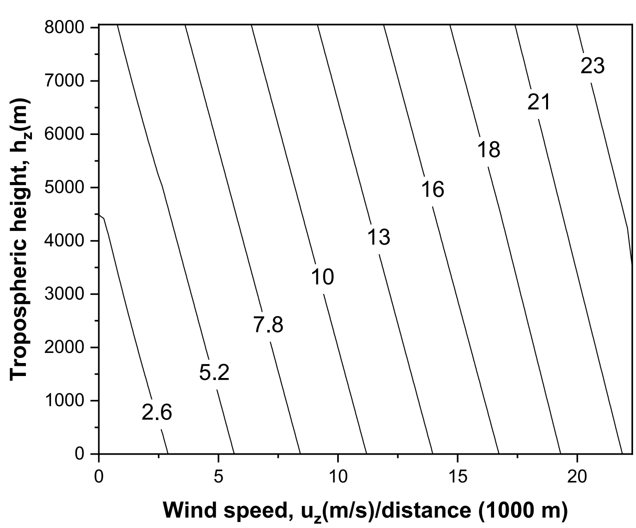


**Fig. 14.** Response of the percentage of solar power gain, $p_z$ (% ) to tropospheric height and wind speed for the Eastern Region.

percentage of solar power gain of 2.5% is possible to attain. This micro percentage of solar power gain of 0.038, 0.071 and 0.144% were measured and computed at stations; 1, 2 and 3 respectively. The corresponding RMSE (0.010, 0.021, 0.020) obtained in Table 5 is quite low. Low percentage of solar power gain results are supported by Amusan and Igbudu (2014), but comparing the percentage of solar power gain by Panjwani and Narejo (2014), who assert range values of 7 to 12%, at tropospheric heights of 0.243 m it is practically impossible to gain such considering that significant percentage of solar power gain at approximately height of 1000 m is 2.5%. Experiment and simulation backed up the present result; hence, the percentage of solar power gain of 2.5% is quite realistic. Further comparison of the present results with that of Chitturi et al. (2018) claimed percentage of solar power gain of 42% height of 1764 m, however, the present work supports about 4% solar power gain. The erroneous generation of Amusan and Igbudu (2014) on insignificant percentage of solar power gain from the earth to the sun is spurious as the present work shows approximately 23% solar power gain in Figs. 13–16. The prospect of having percentage of solar power gain above 23%

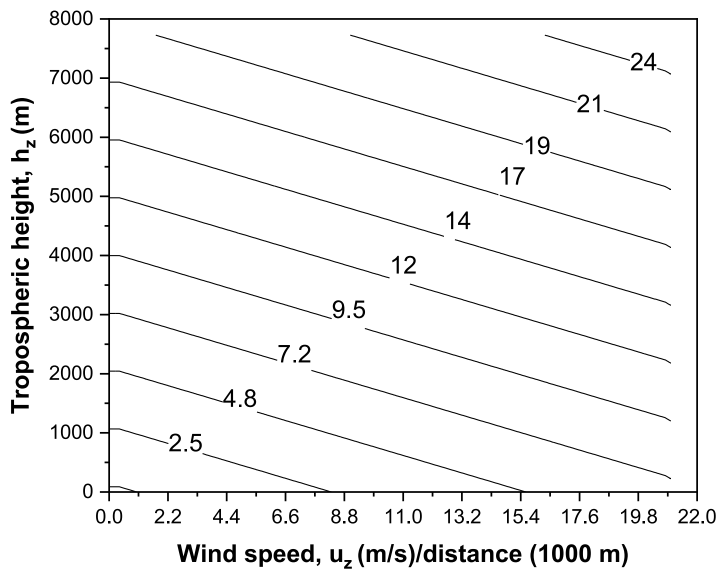


**Fig. 16.** Response of the percentage of solar power gain, $p_z$ (% ) to tropospheric height and wind speed for the Western Region.

is possible by using High Altitude Platforms, HAP (either lighter than air or heavier than air). The present work demystifies the false claims of attaining a high percentage of solar power gain near ground level is practically impossible. However, the prospect of achieving high percentage of solar power gain is possible on the application of HAPs (Aglietti et al., 2008; Gupta et al., 2019). Moreover, it is obvious that high wind speed is attained at high altitude or tropospheric height where air temperature is quite low, this condition accounts for high percentage of solar power gain (Hassan et al., 2021; Deokar et al., 2021; Dwivedi et al., 2020), passive (Ramkiran et al., 2021; Rakino et al., 2019; Wu and Xiong, 2014). The percentage of solar power gain is independent of size and number of solar panel used, but measured power is dependent on the size and number of solar panel. Notably, above ground level energy exploitation is possible with the application of HAPs. Besides, the results in Figs. 13–16 are almost similar, indicates that this result could be used anywhere, provided the elevation is subtracted from the altitude (9200 m) to obtain the tropospheric. The tropospheric height will unveil the possible percentage of solar power gain. Thus, the application of the results goes beyond the present study areas.

Lastly, the economic analysis of acquiring HAP is out of the scope of this work, however, it is technically sound but costly to acquire the HAP.

## 4. Conclusions

This research has accomplished energy exploration above the ground level via modeling and simulations, and experiments. This research is necessitated in bid to explore energy above the ground level for areas not favored with the ground platform in the generation of solar power into electricity. The study reveals that near ground level, about 1000 m could attract a percentage of solar power gain of 2.5%, but at a high altitude of 9200 m, the percentage of solar power gain is prominent to the tune of 23%, however, at altitudes above 9200 m more percentage of solar power gain is possible to achieve.

The model simulation indicated a linear relationship between the tropospheric height and the wind speed. Similarly, a linear relationship exists between the tropospheric height and the percentage of solar power gain. The linear relationship further reveals that the natural wind flow equation, WFE is a linear partial derivative model, describing the potentials; wind speed and the percentage of solar power gain in space with appropriate boundary conditions in three dimensions.

The major results, presenting the percentage of solar power gain as a function of tropospheric height and wind speed are vast in their applications. Outside the study areas, the results are applicable to other study areas having a close elevation as Uganda (1100 m above sea level). Moreover, the application of the results could extend beyond equal elevation; any geographical area having an elevation below 1100 m could conveniently use these results to estimate the possible percentage of solar power gain by subtracting its elevation from 9200 m. Appropriately, access to a higher percentage of solar power gain requires the application of high-altitude platforms (either light-than-air or heavier-than-air), this technology overshadows the influence of topography and other related factors that hinder complete access to solar irradiance by ground platforms.


## Funding

The authors wish to declare that no institution or governmental body sponsored this research.


## CRediT authorship contribution statement

**Stephen Ndubuisi Nnamchi:** Conceptualization, Methodology, Writing – original draft. **Faith Natukunda:** Study design, Validation. **Silagi Wanambwa:** Visualization, Formal analysis, Data curation. **Enos Bahati Musiime:** Writing – review, editing, Software. **Richard Tukamuhebwa:** Resources, Writing – review & editing. **Titus Wanazusi:** Project administration, Writing – review & editing. **Emmanuel Ogwal:** Study design, Writing – review & editing.

## Declaration of competing interest

The authors declare that they have no known competing financial interests or personal relationships that could have appeared to influence the work reported in this paper.

## Data availability

Data will be made available on request.

## Acknowledgment

The authors appreciate Kräuchi and Philipona (2016) for making Radiosonde data available for the study and the rest of the authors featured in the literature.

## References

AccuWeather.com, Ishaka, Bushenyi, 2022. Average wind speed. https://www.accuweather.com/en/ug/ishaka/1895309/current-weather/1895309 (Accessed: 10 May 2022).

Aglietti, G.S., Markvart, T., Tatnall, A.R., Walker, S.J., 2008. Solar power generation using high altitude platforms feasibility and viability. Prog. Photovolt., Res. Appl. 16 (4), 349.

Ahammad, M.J., Rahman, M.A., Alam, J., Butt, S., 2019. A computational fluid dynamics investigation of the flow behavior near a wellbore using three-dimensional Navier–Stokes equations. Adv. Mech. Eng. 11 (9), http://dx.doi.org/10.1177/1687814019873250, 1687814019873250.

Alrwashdeh, S.S., 2018. The effect of solar tower height on its energy output at Ma'an-Jordan. AIMS Energy 6 (6), 959–966.

Amaya, M., 2019. Solar hydrogen production ||. Solar Energy Availabil. 113–149. http://dx.doi.org/10.1016/B978-0-12-814853-2.00005-9.

Amusan, J.A., Igbudu, O., 2014. The effect of pole's height on the output performance of solar power system. Sci. Afr. 13 (2).

Asgharzadeh, A., Marion, B., Deline, C., Hansen, C., Stein, J.S., Toor, F., 2018. A sensitivity study of the impact of installation parameters and system configuration on the performance of bifacial PV arrays. IEEE J. Photovolt. 8 (3), 798–805.

Atkin, P., Farid, M.M., 2015. Improving the efficiency of photovoltaic cells using PCM infused graphite and aluminium fins. Sol. Energy 114, 217–228.

Baldock, N., Mokhtarzadeh-Dehghan, M.R., 2006. A study of solar-powered, high-altitude unmanned aerial vehicles. Aircr. Eng. Aerosp. Technol. 78 (3), 187–193.

Bhattacharya, T., Chakraborty, A.K., Pal, K., 2014. Effects of ambient temperature and wind speed on performance of monocrystalline solar photovoltaic module in Tripura, India. J. Solar Energy 2014, 817078. http://dx.doi.org/10.1155/2014/817078.

Bishoge, O.K., Zhang, L., Mushi, W.G., 2018. The potential renewable energy for sustainable development in Tanzania: A review. Clean Technol. 1 (1), 70–88. http://dx.doi.org/10.3390/cleantechnol1010006.

Blumthaler, M., Ambach, W., Ellinger, R., 1997. Increase in solar UV radiation with altitude. J. Photochem. Photobiol. B: Biol. 39 (2), 130–134. http://dx.doi.org/10.1016/s1011-1344(96)00018-8.

Bogdanov, D., Ram, M., Aghahosseini, A., Gulagi, A., Oyewo, A.S., Child, M., Breyer, C., 2021. Low-cost renewable electricity as the key driver of the global energy transition towards sustainability. Energy 227, 120467. http://dx.doi.org/10.1016/j.energy.2021.120467.

Burmasheva, N., Prosviryakov, E., 2022. Exact solutions to Navier–Stokes equations describing a gradient nonuniform unidirectional vertical vortex fluid flow. Dynamics 2 (2), 175–186. http://dx.doi.org/10.3390/dynamics2020009.

Chandra, S., Agrawal, S., Chauhan, D.S., 2018. Effect of ambient temperature and wind speed on performance ratio of polycrystalline solar photovoltaic module: An experimental analysis. Int. Energy J. 18 (2), 171–180.

Chitturi, S.R.P., Sharma, E., Elmenreich, W., 2018. Efficiency of photovoltaic systems in mountainous areas. In: 2018 IEEE International Energy Conference. ENERGYCON, IEEE, pp. 1–6.

Deokar, V.H., Bindu, R.S., Potdar, S.S., 2021. Active cooling system for efficiency improvement of PV panel and utilization of waste-recovered heat for hygienic drying of onion flakes. J. Mater. Sci., Mater. Electron. 32 (2), 2088–2102. http://dx.doi.org/10.1007/s10854-020-04975-3.

Dwivedi, P., Sudhakar, K., Soni, A., Solomin, E., Kirpichnikova, I., 2020. Advanced cooling techniques of PV modules: A state of art. Case Stud. Therm. Eng. 21, 100674. http://dx.doi.org/10.1016/j.csite.2020.100674.

Eyring, N., Kittner, N., 2022. High-resolution electricity generation model demonstrates suitability of high-altitude floating solar power. IScience 25 (6), 104394. http://dx.doi.org/10.1016/j.isci.2022.104394.

Gupta, S., Duttagupta, S.P., Vachhani, Lee N.A., Mitra, M., 2019. Attitude control of LTA platform for generation of a non-oscillatory solar power. Sol. Energy 189, 131–150. http://dx.doi.org/10.1016/j.solener.2019.07.017-359.

Hasan, A., Sarwar, J., Alnoman, H., Abdelbaqi, S., 2017. Yearly energy performance of a photovoltaic-phase change material (PV-PCM) system in hot climate. Sol. Energy 146, 417–429. http://dx.doi.org/10.1016/j.solener.2017.01.070.

Hassan, H., Yousef, S.M., Abo-Elfadl, S., 2021. Energy, exergy, economic and environmental assessment of double pass V-corrugated-perforated finned solar air heater at different air mass ratios. Sustain. Energy Technol. Assess. 43, 100936. http://dx.doi.org/10.1016/j.seta.2020.100936.

Kräuchi, A., Philipona, R., 2016. Return glider radiosonde for in situ upper-air research measurements. Atmos. Meas. Tech. 9 (6), 2535–2544.

Lee, S., Ryi, S.K., Lim, H., 2017. Solutions of Navier–Stokes equation with coriolis force. Adv. Math. Phys. 2017, http://dx.doi.org/10.1155/2017/704268.

Loria, A.F.R., 2020. Energy geostructures: Theory and application. In: E3S Web of Conferences, Vol. 205. EDP Sciences, p. 01004.

Luo, Z., Huang, Z., Xie, N., Gao, X., Xu, T., Fang, Y., Zhang, Z., 2017. Numerical and experimental study on temperature control of solar panels with form-stable paraffin/expanded graphite composite PCM. Energy Convers. Manage. 149, 416–423.

Mahdi, J.M., Singh, R.P., Al-Najjar, H.M.T., Singh, S., Nsofor, E.C., 2021. Efficient thermal management of the photovoltaic/phase change material system with innovative exterior metal-foam layer. Sol. Energy 216, 411–427. http://dx.doi.org/10.1016/j.solener.2021.01.008.

Majid, M.A., 2020. Renewable energy for sustainable development in India: Current status, future prospects, challenges, employment, and investment opportunities. Energy Sustain. Soc. 10 (1), 1–36.

Maka, A.O., Alabid, J.M., 2022. Solar energy technology and its roles in sustainable development. Clean Energy 6 (3), 476–483. http://dx.doi.org/10.1093/ce/zkac023.

Mundu, M.M., Nnamchi, S.N., Ukagwu, K.J., Peter, B.A., Nnamchi, O.A., Ssempewo, J.I., 2022. Numerical modelling of wind flow for solar power generation in a case study of the tropical zones. Model. Earth Syst. Environ. 1–12. http://dx.doi.org/10.1007/s40808-021-01343-w.

Nnamchi, S.N., Mundu, M.M., Nnamchi, O.A., Onochie, U., Jagun, Z.O., 2022. Differential modelling and simulation of solar power potential: A helio-application of biharmonic model. Model. Earth Syst. Environ. 8 (2), 2383–2400. http://dx.doi.org/10.1007/s40808-021-01232-2.

Nnamchi, O.A., Ndukwu, M.C., Nnamchi, S.N., 2021. Modelling and simulation of multi-coupled heat and mass transfer processes: A case study of solar biomass dryer. Therm. Sci. Eng. Prog. 25, 101007. http://dx.doi.org/10.1016/j.tsep.2021.101007.

Nnamchi, S.N., Nnamchi, O.A., Odebiyi, S.O., Edosa, O.O., Wanazusi, T., 2019. Experimental verification of suitability of insulation testing rig in determining thermophysical properties of insulating materials. Cogent Eng. 6 (1), 1657264.

Oko, C.O.C., Nnamchi, S.N., 2013. Coupled heat and mass transfer in a solar grain dryer. Drying Technol. 31 (1), 82–90. http://dx.doi.org/10.1080/07373937.2012.719561.

Osma, G., Ordóñez, G., Hernández, E., Quintero, L., Torres, M., 2016. The Impact of Height Installation on the Performance of PV Panels Integrated Into a Green Roof in Tropical Conditions ,Vol. 205. WIT Press, Southampton, UK, pp. 147–156.

Owusu, P.A., Asumadu-Sarkodie, S., 2016. A review of renewable energy sources, sustainability issues and climate change mitigation. Cogent Eng. 3 (1), 1167990. http://dx.doi.org/10.1080/23311916.2016.1167990.

Panjwani, M.K., Narejo, G.B., 2014. Effect of altitude on the efficiency of solar panel. Int. J. Eng. Res. General Sci. 2 (4), 461–464.

Pielke Sr, R.A., 2013. Mesoscale Meteorological Modeling. Academic Press.

Radwan, A.G., Khanday, F.A., Said, L.A., 2021. Fractional-Order Modeling of Dynamic Systems with Applications in Optimization, Signal Processing, and Control. Academic Press.

Rakino, S.A., Suherman, S., Hasan, S., Rambe, A.H., 2019. A passive cooling system for increasing efficiency of solar panel output. J. Phys. Conf. Ser. 1373 (1), 012017. http://dx.doi.org/10.1088/1742-6596/1373/1/012017.

Ramkiran, B., Sundarabalan, C.K., Sudhakar, K., 2021. Sustainable passive cooling strategy for PV module: A comparative analysis. Case Stud. Therm. Eng. 27, 101317. http://dx.doi.org/10.1016/j.csite.2021.101317.

Rapp, B.E., 2016. Microfluidics: Modeling, Mechanics and Mathematics. William Andrew.

Rublev, G., Bogdanova, L., Kurbatova, S., Krasnousov, S., Kolmakov, V., 2021. Socio-economic model of sustainable development. In: E3S Web of Conferences, Vol. 244. EDP Sciences, p. 10053.

Sahu, P.P., Swain, A., Sarangi, R.K., 2021. Role of PCM in solar photovoltaic cooling: An overview. In: Proceedings of International Conference on Thermofluids. Springer, Singapore, pp. 245–259.

Seto, D.B., Kristiawan, B., Arifin, Z., 2021. Solar cell cooling with phase change material (PCM) for enhanced efficiency: A review. IOP Conf. Ser. Mater. Sci. Eng. 1096 (1), 012052, https://iopscience.iop.org/article/10.1088/1757-899X/1096/1/012052.

Sharaf, M., Yousef, M.S., Huzayyin, A.S., 2022. Review of cooling techniques used to enhance the efficiency of photovoltaic power systems. Environ. Sci. Pollut. Res. 29, 26131–26159. http://dx.doi.org/10.1007/s11356-022-18719-9.

Shastry, D.M.C., Arunachala, U.C., 2020. Thermal management of photovoltaic module with metal matrix embedded PCM. J. Energy Storage 28, 101312. http://dx.doi.org/10.1016/j.est.2020.101312.

Sodhi, M., Banaszek, L., Magee, C., Rivero-Hudec, M., 2022. Economic lifetimes of solar panels. Procedia CIRP 105, 782–787, https://creativecommons.org/licenses/by-nc-nd/4.0.

Taha, H.E., Gonzalez, C., 2022. What does nature minimize in every incompressible flow. http://dx.doi.org/10.48550/arXiv.2112.12261, arXiv preprint arXiv:2112.12261.

Thadani, H.L., Go, Y.I., 2021. Integration of solar energy into low-cost housing for sustainable development: Case study in developing countries. Heliyon 7 (12), http://dx.doi.org/10.1016/j.heliyon.2021.e08513.
Tucho, G.T., Kumsa, D.M., 2020. Challenges of achieving sustainable development goal 7 from the perspectives of access to modern cooking energy in developing countries. Front. Energy Res. 8, 564104.
Wu, S., Xiong, C., 2014. Passive cooling technology for photovoltaic panels for domestic houses. Int. J. Low-Carbon Technol. 9 (2), 118–126.
Zakšek, K., Podobnikar, T., Oštir, K., 2005. Solar radiation modelling. Comput. Geosci. 31 (2), 233–240. http://dx.doi.org/10.1016/j.cageo.2004.09.018.
Zhang, L., Zhu, W., Du, H., Lv, M., 2021. Multidisciplinary design of high altitude airship based on solar energy optimization. Aerosp. Sci. Technol. 110, 106440. http://dx.doi.org/10.1016/j.ast.2020.106440.